



23 **Abstract**

24 The South Atlantic Ocean plays an important role in the Atlantic meridional overturning  
25 circulation (AMOC), connecting it to the Indian and Pacific Oceans as part of the global  
26 overturning circulation system; yet the detailed time mean circulation structure in this region and  
27 the large-scale spatial pattern of the AMOC variability remain unclear. Using model outputs from  
28 a 60-year, eddying global ocean-sea ice simulation validated against observations at a zonal section  
29 at 34°S, a meridional section at 65°W in the Drake Passage, and a meridional section southwest of  
30 Africa, we show that the upper limb of the AMOC originates primarily from the Agulhas leakage  
31 and that, while the cold Pacific water from the Drake Passage does not contribute significantly to  
32 the AMOC, it does play a role in setting the temperature and salinity properties of the water masses  
33 in the subtropical South Atlantic. We also find that the North Atlantic deep water (NADW) in the  
34 lower limb of the AMOC flows southward as a deep western boundary current all the way to 45°S  
35 and then turns eastward to flow across the Mid-Atlantic Ridge near 42°S, and that the recirculation  
36 around the Vitoria-Trindade seamount chain brings some NADW into the Brazil Basin interior.  
37 Finally, we find that the modeled AMOC variability is coherent on interannual to decadal  
38 timescales from 35°S to about 35°N, where diapycnal water mass transformations between the  
39 upper and lower limbs of the AMOC are expected to be small.

40 **Plain Language Summary**

41 The Atlantic Ocean features a meridional overturning circulation in which the warm water flows  
42 northward in the upper layer and cold water flows southward in the deep. Through South Atlantic  
43 this overturning circulation is connected to the Indian/Pacific Oceans and becomes part of the  
44 global circulation system. The spatial structure and temporal variability of the South Atlantic  
45 circulation remain not well-determined in observations, however, and in this study, we used a

46 numerical model that represented well the observed volume transports at key locations to address  
47 the questions. We showed that the northward-flowing branch of the overturning circulation  
48 originates primarily from the Indian (Ocean) water; the Pacific water does flow into the subtropical  
49 South Atlantic and modifies the temperature and salinity property there. The deep water flows  
50 southward along western boundary all the way to about 45°S and then turns eastward to flow across  
51 the Mid-Atlantic Ridge near 42°S; some deep water also enters the interior of the Brazil Basin  
52 through eddies and recirculation. The variability of the overturning circulation on interannual to  
53 decadal timescales correlates in a wide latitudinal range from 35°S to 35°N, away from the high-  
54 latitude regions where the deep water is formed and upwelled.

## 55 **1. Introduction**

56 In the Atlantic Ocean, warm water from the South Atlantic flows northward in approximately the  
57 upper 1000 meters, loses buoyancy to the atmosphere by cooling *en route* to the northern North  
58 Atlantic, and eventually sinks and returns southward at depth as the cold North Atlantic Deep  
59 Water (NADW). The temperature difference between the upper and lower limbs of this Atlantic  
60 meridional overturning circulation (AMOC) leads to a large northward oceanic heat transport  
61 throughout the entire Atlantic basin, in contrast to the poleward heat transport in the Indo-Pacific  
62 Ocean (e.g., Macdonald and Baringer, 2013). The South Atlantic Ocean, defined here as the area  
63 south of 20°S (Figure 1), plays an important role in that it is through this region where the upper  
64 and lower AMOC limbs are connected to the Indian and Pacific Oceans and are entangled in the  
65 global overturning circulation system (e.g., Gordon, 1986; Broecker, 1991; Schmitz, 1995, 1996;  
66 Richardson, 2008; Talley, 2013). Thus, a comprehensive knowledge of the circulation in this  
67 region is essential to our understanding of the spatial structure and temporal variability of the  
68 AMOC.

69 Significant observations have been made in the last 15 years or so toward quantifying and  
70 monitoring the AMOC in the South Atlantic, particularly along a latitude near 34.5°S (e.g.,  
71 Baringer and Garzoli, 2007; Dong et al., 2009, 2014, 2015; Garzoli et al., 2013; Goes et al., 2015;  
72 Meinen et al., 2013, 2018). These observations, which consist of moorings, expendable  
73 Bathythermograph (XBT), and Argo float measurements, yield a time mean AMOC transport on  
74 the order of 14-20 Sv. They also show that there is significant AMOC variability on several  
75 timescales, similar to that observed by the RAPID array at 26.5°N (e.g., Smeed et al., 2018).  
76 Beyond 34.5°S, however, the observations in the South Atlantic remain sparse and short (in time).  
77 Overall, our understanding of the spatial structure of the time mean circulation is mostly limited  
78 to the schematic of Stramma and England (1999) and even less is known about its temporal  
79 variability.

80 In particular, there is a long-standing debate regarding the source of the upper limb of the AMOC  
81 (Gordon, 2001): whether it originates from the warm, saline Indian waters through the southern  
82 rim of Africa (e.g., Gordon 1986; Saunders and King 1995) or from the cooler, fresher Pacific  
83 water through the Drake Passage (e.g., Rintoul, 1991; Schlitzer, 1996). Although recent studies  
84 seem to favor the warm-water route from the Indian Ocean through the Agulhas leakage (e.g.,  
85 Richardson 2007; Beal et al., 2011), the relative contributions of cold versus warm water are still  
86 uncertain (Garzoli and Matano, 2011; Bower et al., 2019). For example, Rodrigues et al. (2010)  
87 estimated a cold-water contribution of 4.7 Sv based on quasi-isobaric subsurface floats and  
88 hydrographic data. This value is similar to the recent estimate by Rühls et al. (2019) from a  
89 Lagrangian analysis of an eddy-rich model, but it is significantly higher than the historical  
90 estimates of 1-2 Sv estimated from Lagrangian analyses in models or reanalysis (e.g., Speich et  
91 al., 2001; Donners and Drijfhout, 2004; Friocourt et al., 2005; Rousselet et al., 2020). At depth, in

92 the lower limb of the AMOC, much attention has been paid to an eastward flow of the NADW  
93 near 22°S (e.g., Speer et al., 1995; Stramma and England, 1999; Arhan et al., 2003; Hogg and  
94 Thurnherr, 2005; van Sebille et al., 2012; Garzoli et al., 2015). However, the extent of the eastward  
95 penetration in the Angola basin and the exact location where the DWBC turns eastward south of  
96 34°S and flows across the Mid-Atlantic Ridge (MAR) are still debatable. Finally, there is also the  
97 underlying question as to whether the AMOC variability is meridionally coherent throughout the  
98 whole Atlantic (Kelly et al., 2004; Xu et al., 2014).

99 Three-dimensional circulation information beyond the existing observations is required in order to  
100 address the above questions. In this paper, we use a high-resolution numerical model to investigate  
101 in detail the structure of the mean circulation in the South Atlantic as well as the temporal  
102 variability of the AMOC on basin scales. The paper is structured as follows: Section 2 summarizes  
103 the basic features of the numerical simulation. Section 3 compares the modeled large-scale  
104 circulation pattern and the circulation structure with observations at three key observation  
105 locations: 34°S across the South Atlantic, 65°W in the Drake Passage, and along a Prime Meridian-  
106 Good Hope section southwest of Africa (Figure 1). The model results are shown to be in good  
107 agreement with the observed transports and are then used to document the time mean circulation  
108 pattern in the South Atlantic (Section 4) and the latitudinal coherence of the AMOC variability  
109 throughout the Atlantic basin (Section 5). Summary and discussions follow in Section 6.

## 110 **2. Numerical Simulation**

111 The numerical results presented in this study are from a long-term global ocean-sea ice hindcast  
112 simulation performed using the Hybrid Coordinate Ocean Model (HYCOM, Bleck, 2002;  
113 Chassignet et al., 2003), coupled with the Community Ice Code (CICE, Hunke and Lipscomb,  
114 2008). The vertical coordinate of the HYCOM is isopycnic in the stratified open ocean and makes

115 a dynamically smooth and time-dependent transition to terrain following in the shallow coastal  
116 regions and to fixed pressure levels in the surface mixed layer and/or unstratified seas. In doing  
117 so, the model combines the advantages of the different coordinate types in simulating coastal and  
118 open ocean circulation features simultaneously (e.g., Chassignet et al., 2006).

119 The simulation has a horizontal resolution of  $1/12^\circ$  ( $\sim 6$  km in the area of interest) and a vertical  
120 resolution of 36 layers (in  $\sigma_2$ ). It is initialized using the January temperature and salinity from an  
121 ocean climatology (Carnes, 2009) and is forced using the latest surface-atmospheric reanalysis  
122 dataset JRA55 (Tsujino et al., 2018), which has a refined grid spacing of  $\sim 55$  km and temporal  
123 interval of 3 hours and covers the time period of 1958-2018. The surface heat flux forcing is  
124 computed using the shortwave and longwave radiations from JRA55, as well as the latent and  
125 sensible heat fluxes derived from the CORE bulk formulae of Large and Yeager (2004) and the  
126 model sea surface temperature (SST). The surface freshwater forcing includes evaporation,  
127 precipitation, and climatological river runoffs. In addition, the model sea surface salinity (SSS) is  
128 restored toward ocean climatology with a restoring timescale of two months and it is constrained  
129 by an ad hoc assumption of zero global net flux at each time step. The wind stress is calculated  
130 from the atmospheric wind velocity and does not take into account the shear introduced by the  
131 ocean currents. The simulation starts from rest and is integrated over 1958-2018 with no data  
132 assimilation. The horizontal diffusion parameters are listed in Table 1. In this study, we focus on  
133 the last 40 years of the simulation (1979-2018) as being representative of the time-mean circulation  
134 after spin-up (see Figure 2 below).

135 While a detailed evaluation of the global ocean circulation and of the sea ice in the model is  
136 provided in Chassignet and al. (2020), some basic measures are useful. Figure 2 displays the  
137 evolution of the domain averaged potential temperature and total kinetic energy of the world ocean.

138 The model temperature exhibits a weak cooling of  $\sim 0.06^\circ \text{C}$  per century from early 1960s to late  
139 1990s, followed with a 20-year warming of  $\sim 0.11^\circ \text{C}$  per century from 1998 to 2018 (Figure 2a,  
140 domain-averaged salinity is constant because of the zero net freshwater flux constraint). The  
141 modeled warming rate for the last 20 years corresponds to a positive net heat flux of  $\sim 0.50 \text{ W/m}^2$ .  
142 This net heat flux in model is comparable with the estimates of  $0.50 (\pm 0.43) \text{ W/m}^2$  based on the  
143 energy gain at the top of atmosphere for 2001-2010 (Loeb et al., 2012) and  $0.64 (\pm 0.11) \text{ W/m}^2$   
144 based on 0-700 m oceanic heat content change from combined XBT and Argo data for 1993-2008  
145 (Roemmich et al., 2015). The modeled total kinetic energy spins up quickly to  $\sim 35 \text{ cm}^2/\text{s}^2$  in the  
146 first two years and remains on that level for the rest of the integration (Figure 2b). The global  $1/10^\circ$   
147 simulation performed by Maltrud and McClean (2005) using the Parallel Ocean Program (POP)  
148 also reaches a maximum in kinetic energy in the first couple of years and levels off for the rest of  
149 the simulation, except that the energy level is slightly lower at  $25\text{-}30 \text{ cm}^2/\text{s}^2$  (their Figure 1).

150 The sea ice is quantified and monitored in term of sea ice extent, defined as the area with 15% or  
151 higher sea ice concentration. Figure 3 compares the evolution of the modeled sea ice extent in  
152 million  $\text{km}^2$  with the latest results from the National Snow and Ice Data Center (Fetterer et al.,  
153 2017). There is a general agreement between model and data in both the northern and southern  
154 hemispheres and on both seasonal (Figure 3a) and interannual (Figure 3b) timescales. In particular,  
155 as in the observations, the modeled sea ice extent has been decreasing in the northern hemisphere  
156 since the beginning of the observations in 1979. The modeled sea ice extent in the southern  
157 hemisphere, despite having lower annual mean values than observed, is relatively stable or  
158 increases slightly over time and the variability is in good agreement with the observations (Figure  
159 3b).

160 Figure 4 shows the modeled AMOC transport at 26.5°N, defined as the northward trans-basin  
 161 transport above the modeled time mean maximum overturning depth (1000 m). The modeled  
 162 AMOC transport has a mean and standard value of  $14.2 \pm 3.1$  Sv and exhibits a multidecadal  
 163 variability, with low transport in 1970s and high transport in 1990s (Figure 4a). The modeled mean  
 164 AMOC transport in 2004-2017 is 13.6 Sv, which is 3.7 Sv or  $\sim 20\%$  lower than the 17.3 Sv based  
 165 on the RAPID data (updated from Smeed et al., 2018). The modeled AMOC variability, however,  
 166 compares well to the observations: On interannual timescales, the magnitude of the AMOC  
 167 variability is lower in model than in the RAPID observations (standard deviation of 1.0 Sv versus  
 168 1.5 Sv), but the two have a similar time evolution that is also consistent with the meridional heat  
 169 transport anomaly of Trenberth et al. (2019) based on independent observations (Figure 4b). On  
 170 seasonal timescale, the modeled AMOC variability is similar to the RAPID observations in both  
 171 magnitude (multi-year averaged monthly mean transports give a standard deviation of 1.6 Sv in  
 172 both time series) and phase, with low transports in January-June and high transports in July-  
 173 December (Figure 4c).

174 Table 1. Viscosity and diffusion coefficients used in the  $1/12^\circ$  global ocean simulation

Parameters	Values
Laplacian coefficient for momentum	$20 \text{ m}^2 \text{ s}^{-1}$
Biharmonic diffusive velocity for momentum	$1 \text{ cm s}^{-1}$
Biharmonic diffusive velocity for layer thickness	$1.5 \text{ cm s}^{-1}$
Laplacian diffusive velocity for tracers	$0.5 \text{ cm s}^{-1}$

175

### 176 **3. Model validation**

177 In this section, we first evaluate the large-scale surface circulation and then quantify the modeled  
178 transport structure at three sections in the South Atlantic: 34°S, 65°W in the Drake Passage, and a  
179 Prime Meridian-Good Hope section southwest of Africa (Figure 1). Significant observations have  
180 been conducted at these locations and they provide a benchmark for evaluating the realism of the  
181 modeled transports, which will be used to document the transport structure of the South Atlantic  
182 in Section 4.

#### 183 **3.1 The surface circulation pattern**

184 Figure 5 compares the observed and modeled mean sea surface height (SSH), SSH variability, and  
185 eddy kinetic energy (EKE) of the surface currents in the South Atlantic. The observed mean SSH  
186 (Figure 5a) is from the latest mean dynamic topography climatology CNES-CLS18 (Mulet et al.  
187 2020) while the SSH variability (Figure 5c) and surface EKE (Figure 5e) are derived from the  
188 AVISO data over the 1993-2018 period, the same time period used for the model results. In the  
189 western side of the domain, part of the Antarctic Circumpolar Current (ACC) turns north after  
190 passing the Drake Passage and becomes the Malvinas Current (also called the Falkland Current).  
191 The latter continues to flow northward along the continental shelf of Argentina until it meets the  
192 southward flowing Brazil Current south of the Rio de la Plata estuary near 36°S. The confluence  
193 of these two western boundary currents with opposite directions and very different properties  
194 (warm salty subtropical water versus cold fresh subantarctic water) leads to numerous high-energy  
195 eddies and thus strong variability in this so-called Brazil-Malvinas confluence zone (Figures 5c-  
196 f). In the south, the ACC is mostly zonal and exhibits a contracted (stronger) front in two areas:  
197 one near 40°W south of the Zapiola Drift and the other near 10°W over the MAR. Overall, there  
198 is a good agreement between the model and the observations in the western and southern part of

199 the domain, with the exception of a slightly lower model SSH variability offshore in the Brazil-  
200 Malvinas confluence zone near 40°S.

201 West of Africa, the model results exhibit a narrow tongue of high SSH variability/EKE that extends  
202 farther northwest into the South Atlantic than in observations. This is a common feature for many  
203 eddying models (e.g., Maltrud and McClean, 2005; Dong et al. 2011; van Sebille et al. 2012) where  
204 the Agulhas rings that shed from the Agulhas retroflection and translate northwestward into the  
205 South Atlantic follow a regular pathway and are too energetic. Plots of the SSH variability for both  
206 the model and the observations along the Prime Meridian over the observational period of 1993-  
207 2018 in Figure 6 show that the modeled rings are stronger and pass the Prime Meridian within a  
208 smaller latitudinal range than in the observations.

### 209 **3.2 Transport across 34°S**

210 Figures 7a-d display a vertical section of the time-mean potential temperature  $\theta$  and salinity  $S$  at  
211 34°S. The observations are based on the gridded monthly Argo profiles (2004-2014) for the upper  
212 2000 m and the World Ocean Atlas 2013 (WOA13, Locarnini et al. 2013; Zweng et al. 2013)  
213 below 2000 m; the model results are 40-year means from 1979 to 2018. The water column at this  
214 latitude can be divided into four density layers of water masses that are characterized most clearly  
215 by its salinity ( $\theta$  decreases monotonically): saline near surface water ( $\sigma_2 < 35.65 \text{ kg m}^{-3}$ ), fresh  
216 Antarctic Intermediate Water (AAIW,  $35.65 < \sigma_2 < 36.58$ ), saline NADW ( $36.58 < \sigma_2 < 37.12$ ), and  
217 fresh Antarctic Bottom Water (AABW,  $\sigma_2 > 37.12$ ). There is a good agreement in the  $\theta$  and  $S$   
218 distributions, such as the warm/saline anomaly in 2000-3000 m depth range associated with the  
219 NADW in the DWBC. For a more quantitative comparison, Figures 7e-f display the volumetric  $\theta$ -  
220  $S$  diagram along 34°S for both observations and model results. The color shading is volume

221 percentage of water mass calculated with a  $\Delta\theta \times \Delta S$  grid resolution of  $0.1^\circ\text{C} \times 0.02$  psu and the  
222 circled black/red lines are the volume weighted  $\theta$ -S values calculated for each of the HYCOM  
223 density layers. AAIW occupies  $\sim 20\%$  of the volume at this latitude in both the observations and  
224 model results, and this water mass as a whole is  $0.35^\circ\text{C}$  warmer and  $0.11$  psu saltier in the model  
225 than in observations (the maximum  $\theta$ -S difference is  $\sim 0.8^\circ\text{C}$  and  $0.18$  psu for an individual density  
226 layer). Above the AAIW, the modeled near surface water is about  $0.8^\circ\text{C}$  warmer than observed  
227 and its salinity is very close to the observations (error on the order of  $0.02$  psu); below the AAIW,  
228 the model results exhibit more AABW and less NADW than in WOA13, but the differences in  $\theta$ -  
229 S properties are small ( $0.1^\circ\text{C}$  and  $0.02$  psu, respectively). Overall, the modeled water properties  
230 are consistent with observations.

231 The time mean meridional velocity across  $34^\circ\text{S}$  and the corresponding volume transports for the  
232 four water masses defined above are shown in Figure 8. The observations consist of geostrophic  
233 transports derived from  $\theta/S$  profiles (Argo-WOA13 data) and Ekman transports from the wind  
234 stress; see Dong et al. (2014) for details. The model results are 40-year means (1979-2018). The  
235 main circulation at this latitude consists of the South Atlantic subtropical gyre (southward Brazil  
236 Current near the western boundary and northward interior flow) and the AMOC (northward  
237 Bengula Current near the eastern boundary and southward DWBC near the western boundary).  
238 Quantitatively, the total transport of the southward western boundary current is about  $42$  Sv ( $12$ ,  
239  $8$ , and  $22$  Sv for the surface water, AAIW, and NADW, respectively) in model, compared to  $45$   
240 Sv ( $7$ ,  $8$ , and  $30$  Sv for the surface water, AAIW, and NADW, respectively) in observations. In the  
241 surface water and AAIW layers, the observed subtropical gyre extends from the western boundary  
242 to  $0$ - $10^\circ\text{E}$ , while the northward-flowing AMOC component occupies the rest of the section to the  
243 coast of Africa. The modeled transport pattern is similar to the observations, except that the regular

244 pathway of the Agulhas rings leads to a north/south circulation in the Cape Basin. In the NADW  
245 layer, both observations and model results show a strong southward DWBC west of 40°W and a  
246 northward return flow east of 40°W. Note that the DWBC is quite wide at this latitude and that the  
247 transport obtained by Meinen et al. (2017), 15 Sv west of 44.5°W, does not include the full DWBC  
248 (near 30 Sv in Argo-WOA13 based observations and 22 Sv in model). The return flow is mostly  
249 localized over the Walvis Ridge. In the Cape Basin, both the Argo-WOA13 based observations  
250 and the model show a recirculation of the NADW which is consistent with the recent results of  
251 Kersalé et al. (2019) derived from moored CPIES-Current and Pressure recording Inverted Echo  
252 Sounders. This deep recirculation is likely driven by eddy activity in the upper ocean and is  
253 stronger in the model (see Figure 5). The pattern does not appear to be affected by the fact that the  
254 modeled Agulhas eddies follow a regular pathway. The modeled AABW transport is about 2 Sv  
255 in the western basin, much less than the 4-7 Sv estimated in observations (e.g., Hogg et al., 1982;  
256 Speer and Zenk, 1993). There is no AABW transport in the Argo-WOA13 based results.

257 The meridional flows shown in Figure 8 have a significant barotropic component and the  
258 baroclinic nature of the AMOC, i.e., northward flows in the upper limb and southward flows in  
259 the lower limb, becomes apparent only when integrated across the basin (Figure 9). The zonally  
260 integrated mean transport streamfunction with respect to the depth  $z$  shows a maximum  
261 overturning depth near 1300 m in both observations and model results (Figure 9a). The modeled  
262 mean AMOC transport is 14.7 Sv. This value agrees with the recent SAMOC estimate based on  
263 six years of moored observations at the western and eastern boundaries (14.7 Sv, Meinen et al.,  
264 2018), but is significantly lower than the estimates based on XBT transects (18 Sv, Dong et al.,  
265 2009; Garzoli et al., 2013) and Argo-WOA13 (20 Sv, Dong et al., 2014). With respect to density  
266 (Figure 9b), the northward AMOC limb is above the density surface ( $\sigma_2$ ) 36.58 kg/m<sup>3</sup> and the

267 southward limb below. The modeled mean AMOC transport in density space is 15.8 Sv, compared  
268 to 18.7 Sv based on Argo-WOA13. The modeled northward AMOC limb consists of 9.0 Sv of  
269 warm surface water transport and 6.8 Sv of AAIW transport, compared to 12.7 and 6.0 Sv,  
270 respectively, in the Argo-WOA13 observations. This leads to a lower meridional heat transport  
271 (MHT) of  $0.36 \pm 0.23$  PW in the model, compared to  $0.68 \pm 0.24$  PW in the Argo-WOA13  
272 observations. The historical estimates of the MHT near this latitude are 0.22-0.62 PW (see Table  
273 29.3 in Macdonald and Baringer, 2013).

274 At 34°S, the modeled AMOC transport variability is lower than in the observations on both  
275 interannual and seasonal timescales (Figure 10): On interannual timescale, the model AMOC  
276 transports have a standard deviation of 1.0 Sv in 2004-2014, compared to 1.9 Sv in Argo-WOA13  
277 based observations for the same period and 2.6 Sv in SAMOC results (Meinen et al., 2018) for a  
278 shorter, 6-year period (2009-2010 and 2013-2017). The time evolution of the modeled AMOC  
279 variability is similar to the Argo-WOA13 based observations in 2004-2012 but differ after 2012  
280 (Figure 10a); note the Argo-WOA13 and SAMOC observations also differ in 2013-2014 when the  
281 two observations overlap. On seasonal timescale, the modeled AMOC transports have a standard  
282 deviation of 2.2 Sv, compared to 3.3 Sv in the Argo-WOA13 and 2.9 Sv in the SAMOC  
283 observations. Although the magnitude is lower, the phase of the modeled seasonal variability is  
284 consistent with the Argo-WOA13 and the SAMOC based observations (Figure 10b).

### 285 **3.3 Transport through the Drake Passage at 65°W**

286 The Drake Passage is an ACC chokepoint and the place where long-term sustained monitoring  
287 programs have been conducted; see Meredith et al. (2011) for a review of historical observations.  
288 The canonical full-depth volume transport is  $133.8 \pm 11.2$  Sv, based on year-long current meter  
289 mooring and cruise data obtained during the International Southern Ocean Studies (ISOS,

290 Whitworth, 1983; Whitworth and Peterson, 1985). However, based on a combination of moored  
291 current meter data from the DRAKE program (2006-2009) and satellite altimetry data (1992–  
292 2012), Koenig et al. (2014) estimated a higher full-depth transport of  $141 \pm 2.7$  Sv. More recently,  
293 Chidichimo et al. (2014) and Donohue et al., (2016) estimated an even higher mean ACC transport  
294 of 173.3 Sv, based on the high-resolution moored bottom current and pressure measurements of  
295 the cDrake program (2007-2011).

296 The modeled mean ACC transport is 157.3 Sv, about the average of the estimates from DRAKE  
297 and cDrake programs. In a detailed analysis of the modeled ACC transport through the Drake  
298 passage, Xu et al. (2020) found that a) the modeled ACC transport in the upper 1000 m of the  
299 Drake Passage is in excellent agreement with that of Firing et al. (2011) based on shipboard  
300 acoustic Doppler current profiler (SADCP) transects, and b) the modeled exponentially decaying  
301 transport profile is consistent with the profile derived from the repeat hydrographic data from  
302 Cunningham et al. (2003) and Meredith et al. (2011). By further comparing the model results to  
303 the cDrake and DRAKE observations, Xu et al. (2020) concluded that the modeled 157.3 Sv was  
304 representative of the time-mean ACC transport through Drake Passage. The cDrake experiment  
305 overestimates the barotropic contribution in part because the array undersampled the deep  
306 recirculation in the southern part of the Drake Passage, whereas the DRAKE experiment  
307 underestimates the transport because the surface geostrophic currents yielded a weaker near-  
308 surface transport than implied by the SADCP data.

309 The modeled mean zonal velocity through the Drake Passage at  $65^\circ\text{W}$  and the corresponding  
310 volume transports for the four density layers defined earlier (surface water, AAIW, NADW,  
311 AABW) are shown in Figure 11a. The ACC at this longitude exhibits four high velocity cores  
312 (indicated by arrows in Figure 11a), corresponding to the ACC southern boundary (SBby, south

313 of 63°S), the southern ACC Front (SACCF, at 61-62°S), the Polar Front (PF, at 58-60°S), and the  
314 Sub-Antarctic Front (SAF, at 55-55°S). These modeled fronts are at similar locations as in Orsi et  
315 al. (1995) based on hydrographic surveys and in other studies based on sea surface height data  
316 (e.g., Sallée et al., 2008; Sokolov and Rintoul, 2009; Kim and Orsi, 2014).

317 The modeled monthly mean and 12-month moving averaged ACC transports have a standard  
318 deviation of 5.2 Sv and 2.3 Sv, respectively (Figure 12a). These numbers are relatively small  
319 compared to the long-term mean value of 157.3 Sv. The seasonal variability of the ACC transports  
320 is also small (with a standard deviation of 1.5 Sv) and exhibits a biannual pattern (Figure 13b).  
321 These results agree with the observations in Koenig et al. (2016).

#### 322 **3.4 Transport across the Prime Meridian-Good Hope transect**

323 The wide ocean gap between Antarctica and the southern tip of Africa makes it difficult to fully  
324 measure the transport and its spatial structure. Observations have been collected mostly along the  
325 Prime Meridian (e.g., Whitworth and Nowlin 1987; Klatt et al. 2005) from Antarctica to  
326 approximately 50°S and the Good Hope line from 0°E, 50°S to the Cape of Good Hope, South  
327 Africa (e.g., Legeais et al., 2005; Gladyshev et al., 2008; Swart et al., 2008). We refer to the  
328 combination of these two sections as the Prime Meridian-Good Hope (PM-GH) transect (Figure  
329 1). The modeled net transport through PM-GH (158.5 Sv) is essentially the same as the net  
330 transport through the Drake Passage because of mass conservation, except for an additional 1.2 Sv  
331 from the Pacific-to-Atlantic Bering Strait throughflow.

332 The modeled circulation along the PM-GH section (Figure 11b) can be divided into three regimes:  
333 i) Weddell gyre south of 55.5°S. There are two eastward and two westward jets that form the  
334 Weddell gyre. The two westward jets are found along the Antarctic Slope and the Maud Rise (MR)

335 near 64°S, whereas the two eastward jets are found near 58-59°S and along the southern boundary  
336 (SBdy) of the ACC at 55.5°S right south of the Southwest Indian Ridge (SIR). This modeled jet  
337 pattern is consistent with the observations of Klatt et al., (2005, their Figures 4-5). The time mean  
338 transport of the modeled Weddell gyre is 48.2 Sv, compared to  $56 \pm 8$  Sv estimated in Klatt et al.  
339 (2005).

340 ii) ACC from 55.5°S to 40°S. The modeled ACC exhibits high-velocity cores associated with the  
341 SACCF (52°S), PF (50.4°S and 48°S), SAF (44.6°S), and the subtropical front (STF, 42°S)  
342 respectively. These front positions are close to the observations based on repeat CTD/XBT  
343 transects in this region (Swart et al. 2008, their Table 3). Note that the PF at this location is split  
344 into two fronts, with the elevated eastward velocity between 47°S and 49°S corresponding to its  
345 northern expression (Swart et al. 2008; Gladyshev et al. 2008). The modeled STF is much weaker  
346 than any of the other ACC fronts as in the observations. The modeled mean ACC transport across  
347 the PM-GH transect, defined as the transport from 55.5°S to 40°S including the STF as in Orsi et  
348 al., (1995), is 175 Sv, compared to 147-162 Sv estimated from CTD transects (Whitworth and  
349 Nowlin, 1987; Legeais et al., 2005; Gladyshev et al., 2008). The modeled baroclinic transport is  
350 101.2 Sv above 2500 m, compared to 84.7-97.5 Sv derived from repeated hydrographic surveys  
351 and in combination with satellite altimetry data (Legeais et al., 2005; Swart et al., 2008).

352 iii) Agulhas retroflexion and leakage north of 40°S. The model results show a pair of eastward  
353 and westward flows associated with the Agulhas retroflexion and Agulhas Current. The 'net'  
354 transports north of 40°S is 9.3 and 7.9 Sv westward for the surface water and AAIW, respectively.  
355 Thus, the Agulhas leakage in model provides slightly more transport than the 15.8 Sv in upper  
356 AMOC.

357 The modeled transport across the full PM-GH transect decreases with depth and is eastward above  
358 4000 m (blue line in Figure 13a). There is a weak westward flow below 4000 m. When compared  
359 to the vertical structure of the transport in the Drake Passage (green line in Figure 13a), the  
360 eastward transport through PM-GH transect is weaker in the 0-1000 m range and stronger in the  
361 1000-4000 m range. This is due, in a large part, to the contributions to the northward-flowing upper  
362 limb and from the southward-flowing lower limb of the AMOC (red line in Figure 13a).

363 The modeled net transports into and out of the region bounded by the 34°S, Drake Passage, and  
364 PM-GH sections (see Figure 1) is shown in Figure 13b. There is a net outflow above about 1400 m  
365 and below 3900 m and a net inflow between these two depths. The result implies a maximum  
366 upwelling transport of 5.6 Sv across 1400 m, consistent with the picture put forward by Schmitz  
367 (1995) and Talley (2013) that the Southern Ocean is a key upwelling region for NADW. The net  
368 transport in Figure 13b also implies a downward transport of 1.7 Sv across 3900 m, representing  
369 AABW formation in the model within the region bounded by the 34°S, Drake Passage, and PM-  
370 GH sections.

#### 371 **4. Water mass transformations and circulation pathways in the South Atlantic Ocean**

372 In the previous section, we showed that the model is able to represent the basic circulation features  
373 of the South Atlantic and the Southern Ocean and volume transports consistent with the  
374 observations. In this section, we use the model results to address the questions raised in the  
375 introduction. In subsection 4.1, we focus on the diapycnal water mass transformations associated  
376 with the upwelling as shown in the previous section and, in subsection 4.2, we focus on the  
377 circulation pathways of the upper and lower limbs of the AMOC.

378

**379 4.1 Diapycnal water mass transformations**

380 Similar to Figure 13b, Figure 14a shows the net transports into and out of the region bounded by  
381 the 34°S, 65°W, and PM-GH sections, but with respect to density layers. The positive transports  
382 (in gray bars) denote water flowing into the region (mostly NADW, but also some near surface  
383 water) which is transformed and exits the region in another density class (negative transports in  
384 white bars): in AABW and between the surface water and AAIW. A downward integration of these  
385 layered transports gives the net transport between the sea surface and a given density surface, and  
386 the difference between this integrated net transport and the change of the volume above the density  
387 surface over time gives the total diapycnal water mass transformation (black line in Figure 14b)  
388 taking place in the region across the given density surface; see Xu et al. (2018) for a more detailed  
389 discussion on water mass transformation in the upper North Atlantic.

390 The model results in Figure 14b show significant diapycnal transformations in the region bounded  
391 the 34°S, 65°W, and PM-GH sections: About 12 Sv water in the density range of 36.13-37.0 (6 Sv  
392 in NADW and 6 Sv in lower AAIW) is transformed toward light water across the density surface  
393 of 36.13, which means that a significant part of the AMOC closure takes place within the Atlantic  
394 sector of the Southern Ocean. When compared to the transformations that are driven directly by  
395 the surface buoyancy fluxes (dashed black line in Figure 14b) and calculated from the surface  
396 density fluxes and surface density using the thermodynamic method (e.g., Walin 1982; Speer and  
397 Tziperman, 1992; Brambilla et al., 2008; Langehaug et al., 2012; Xu et al., 2018), we find that the  
398 surface-forced transformation accounts for most of the diapycnal transformation in the South  
399 Atlantic region bounded by the above three sections.

400

**401 4.2 Circulation pathways of the upper and lower limb of the AMOC****402 a) Upper limb (surface water and AAIW)**

403 The upper (northward) limb of the AMOC consists of two density layers: the surface water  
404 ( $\sigma_2 < 35.65$ ) and the AAIW ( $35.65 < \sigma_2 < 36.58 \text{ kg m}^{-3}$ ). The modeled 40-year (1979-2018) mean  
405 horizontal circulation for these two layers is displayed in Figures 15 and 16, respectively. For the  
406 surface water (Figure 15), the AMOC component flows directly northwestward from the Agulhas  
407 Leakage into the South Atlantic (red streamlines); the subtropical gyre of the South Atlantic  
408 (orange lines) flows counter-clockwise and separates the northward-flowing AMOC component  
409 and the eastward-flowing ACC. There is almost no surface water in the ACC coming from the  
410 Pacific Ocean (pink lines) and it does not contribute directly to the AMOC.

411 The modeled circulation pattern of the AAIW (Figure 16) is similar to the surface water (Figure  
412 15), but it shows a meridionally more confined subtropical gyre (orange lines) and a larger  
413 contribution to the ACC from the Pacific Ocean (pink lines). There is an indication of a ‘supergyre’  
414 connecting the subtropical gyres of the South Atlantic and Indian Oceans, which would further  
415 prevent a direct contribution of water mass from the ACC into the upper limb of the AMOC. The  
416 patterns of modeled mean circulation in Figures 15 and 16 are similar to the schematic of Stramma  
417 and England (1999, their Figures 3-4), except for the recirculation in the Cape Basin which is a  
418 consequence of the unrealistic pathways of the modeled Agulhas eddies (see Figures 5 and 6 and  
419 discussion in subsection 3.1).

420 The model time-mean circulation in Figure 16 suggests that the Pacific AAIW does not directly  
421 contribute to the upper limb of the AMOC. But this does not necessarily imply that there is no  
422 contribution by the time-varying part of the circulation, e.g., eddies and meanders. To further  
423 quantify the combined contribution of the mean flow and eddies by the various water mass sources,

424 we examine the water properties of the northward flow in the South Atlantic, by projecting the  
425 northward transports (in Sv) on potential temperature-salinity ( $\theta$ -S) plane and comparing their  
426 properties with the water masses from the Pacific and the Indian Oceans (Figure 17). The Pacific  
427 AAIW that flows northward across 45°S is much fresher than the Indian AAIW that flows  
428 westward across the GH section (Figures 17a-b). The AAIW that flows northward across 34°S and  
429 30°S is a combination of these two sources (Figures 17c-d): At 34°S, 7.8 Sv of AAIW is fresher  
430 than 34.46 (Pacific) and 9.6 Sv is saltier than 34.46 (Indian). At 30°S, the Pacific contribution  
431 ( $S < 34.46$ ) decreased to 3.6 Sv whereas the Indian contribution stayed approximately constant at  
432 9.0 Sv. Further north at 25°S and 20°S (Figure 17e-f), the northward-flowing AAIW does not have  
433 any distinct component of the Pacific origin, suggesting that the main contribution of the Pacific  
434 AAIW in the South Atlantic is to the subtropical gyre, not to the AMOC. However, the northward-  
435 flowing AAIW at 20-25°S is slightly fresher than that at GH (the transport-weighted AAIW  
436 salinity is 34.56 at 20-25°S versus 34.60 at GH). This suggests that some mixing of the Indian  
437 AAIW with the Pacific AAIW takes place in the South Atlantic.

438 To further study the contribution of Pacific AAIW not represented in the mean circulation (i.e.,  
439 contributions by eddies), we released numerical particles into the model AAIW density layers in  
440 the Drake Passage and tracked their trajectories using the modeled daily velocity fields and the  
441 Lagrangian Ocean analysis toolbox OceanParcels (Delandmeter and van Sebille, 2019). The  
442 particles were released across the Drake Passage at 58°W every 5 days in 1987 and 1988 and were  
443 tracked for 30 years. Similar to Blanke et al. (1999), the number of particles released at each grid  
444 point on the section is proportional to the model transport at that location. Each particle is tacked  
445 with a small partial volume transport ( $< 0.02$  Sv) such that the cumulative volume transport of all  
446 the particles reflects the instantaneous total transport for the AAIW layers through the Drake

447 Passage each time they are released. A total of 597,566 particles were released and only 36,348  
448 (6.1%) of them made it north past 34°S after 30 years. This number decreases progressively as one  
449 moves further north with just 12,554 (2.1%) reaching 6°S. All particles crossing 6°S are considered  
450 to be part of the AMOC (e.g., Rühls et al. 2019) and Figure 18a displays the likelihood that one of  
451 these particles went through a given location in the South Atlantic over the 30 years. The figure  
452 shows that a) most of the particles (95%) that reached north of 6°S originated within the  
453 Subantartic Front (SAF) of the ACC that is north of 56.6°S along 58°W, and b) their trajectories  
454 are mostly confined to the western boundary, except for the region between 40°S and 30°S where  
455 most of the particles are entrained in the interior before moving back westward.

456 The volume transport carried by all the particles that across a given latitude, divided by the number  
457 of releases, provides an annual mean “Lagrangian” AAIW transport from the Drake Passage.  
458 Figure 18b displays the AAIW transports across several latitudes from 34°S to 6°S as a function  
459 of time. The AAIW transport across 34°S and 30°S reaches a steady state after 20-25 years at about  
460 3.3 and 2.9 Sv, respectively. This transport decreases as one moves further north with only 1.0 Sv  
461 across 6°S after 30 years. This transport value has not yet reached a steady state, but an exponential  
462 fit using the last 15 years provides a steady state value of ~1.3 Sv. This contribution is close to the  
463 latest estimate of 2 Sv by Rousselet et al. (2020) that is derived using the ECCOV4 (Estimating the  
464 Circulation and Climate of the Ocean). It is, however, significantly smaller than the 4.7 Sv  
465 estimated by Rühls et al. (2019) using a high-resolution ocean simulation.

#### 466 **b) Lower limb (NADW)**

467 Figure 19 shows the modeled mean circulation for the NADW layer ( $36.58 < \sigma_2 < 37.12$ ). The  
468 modeled NADW flows southward as a DWBC along the continental slope of the Brazil and

469 Argentine Basins, all the way to about 40°S where it encounters the northward-flowing deep  
470 Falkland Current. The NADW continues to flow southward (now offshore of the deep Falkland  
471 Current) to about 45°S where it meanders and flows eastward south of the Zapiola Drift (Rise).  
472 This modeled NADW pathway is similar to the one described in the schematic of Stramma and  
473 England (1999, their Figure 5) and is consistent with pathways derived from salinity, oxygen, and  
474 other tracers such as CFC (e.g., Koltermann et al., 2011; Garzoli et al., 2015). There is a strong  
475 counterclockwise flow around the Zapiola Drift (Figure 19) with a transport of approximately 25  
476 Sv. For the full water column, the modeled long-term mean transport for this Zapiola anticyclone  
477 is about 55 Sv, consistent with the long-term mean transport of 50 Sv estimated by Saraceno et al.  
478 (2009) using observed mean dynamic topography (MDT). Higher transports have been estimated,  
479 e.g., 80 Sv by Saunders and King (1995) using on CTD/ADCP surveys and 124 Sv by Colin de  
480 Verdère and Ollitrault (2016) using Argo float data. Some of these differences may be due to the  
481 high variability in the transport on intraseasonal to interannual timescales (e.g., Saraceno et al.,  
482 2009).

483 South of the equator, there are complex recirculation patterns in the Brazil Basin, especially around  
484 the Vitoria-Trindade Seamount Chain near 20°S (Hogg and Owens, 1999), that carry NADW from  
485 the DWBC toward the interior of the basin and lead to high salinity all the way to the MAR in both  
486 the observations (WOCE lines A09 and A095) and the model (Figure 20). The model exhibits a  
487 zonal flow of about 2 Sv across the MAR near 22°S (Figures 19&21), which agrees with the 2 to  
488 5 Sv estimated from observations by Warren and Speer (1991), Speer et al. (1995), Hogg and  
489 Thurnherr (2005), and Garzoli et al. (2015). East of the MAR, the modeled NADW flow turns  
490 northward and circulates around the Angola Basin as in the schematic proposed by Hogg and  
491 Thurnherr (2005). Arhan et al. (2003), however, have a much higher transport (10.7 Sv) across the

492 MAR with the NADW flowing eastward across the Angola Basin and southeastward into the Cape  
493 Basin. Both the observed and modeled salinity distributions at 2500 m (Figure 20) show that  
494 between 20 and 25°S, there is a large salinity difference between the east and west of the MAR  
495 (A15 and A14 WOCE lines, respectively). This does not support Arhan et al. (2003)'s depiction  
496 of a high-salinity NADW transport across the MAR all the way to the eastern boundary. In a  
497 numerical study performed with the JAMSTEC OFES (OGCM for the Earth Simulator) model,  
498 van Sebille et al. (2012) did find a continuous NADW flow east of the MAR, but the OFES model  
499 also exhibited a continuous high salinity tongue (not shown here) that extends eastward across the  
500 entire Angola Basin and southeastward into the Cape Basin, a result that is not supported by the  
501 observations and likely an outcome of the unrealistic modeled zonal flow east of the MAR.

502 Figure 21 also shows that in NADW density range there are weak westward currents across the  
503 MAR south of 22°S which lead to a lower salinity (modeled and observed) in the west basin near  
504 30°S (along A10) when compared to 20-25°S (A09 and A095). Overall, there is no net transport  
505 of NADW across the MAR between 20 and 40°S, thus most of the eastward NADW transport  
506 occurs near 42°S where it joins the ACC water of the same density range ( $36.58 < \sigma_2 < 37.12$ ). The  
507 NADW/ACC streamlines turn northward when approaching the MAR and southward after  
508 crossing the MAR. This meridional shift can be explained by the conservation of potential  
509 vorticity,  $f/h$ , i.e., a decrease in thickness  $h$  when approaching the MAR leads to a northward shift  
510 to reduce the planetary rotation  $f$  so that  $f/h$  is constant and vice versa. Because the MAR is slanted  
511 in a northwest-to-southeast direction in this area, the northward and southward shifts at different  
512 latitude/longitude led to a contraction of the front near 10°W, which can be clearly seen in the SSH  
513 for both model and observations (Figure 5).

514

**515 5. Latitudinal coherence of the AMOC variability**

516 The previous two sections described in detail the mean structure of the AMOC in the South  
517 Atlantic. In this section, we document its variability on seasonal to decadal time scales and address  
518 the question as to whether the AMOC variability is meridionally coherent throughout the whole  
519 Atlantic (Kelly et al., 2004; Xu et al., 2014). Using hydrography and satellite data with a box  
520 model, Kelly et al. (2014) suggested that the meridional heat transport anomalies (closely  
521 correlated with the strength of the AMOC) are highly coherent from 35°S to 40°N on interannual  
522 timescales.

523 The power spectral density of the modeled AMOC variability is shown in Figure 22 for ten  
524 different latitude bands between 35°S and 65°N. On timescales from one to twenty years  
525 (interannual and decadal), there is not a distinct period that the AMOC variability shows a high  
526 energy signal at all latitude bands. The power spectra distribution is similar across all latitude  
527 bands on timescales longer than 20 years, which is to be expected given that the 60-year integration  
528 is too short to truly quantify the multi-decadal variability. The only spectral peak that occurs across  
529 all latitude bands is the annual signal associated with the seasonal cycle of the atmospheric forcing.  
530 The power spectra only tell us the time scales where energy is concentrated and do not provide  
531 information on its spatial structure. In order to obtain a spatial picture of the AMOC variability on  
532 different timescales, we use the ensemble empirical mode decomposition (EEMD, Wu and Huang,  
533 2009) to decompose the modeled AMOC transport time series (1958-2018) at individual latitudes  
534 into a number of amplitude-frequency modulated oscillatory components (termed as the intrinsic  
535 mode functions, or IMFs) successively from the highest to the lowest frequencies, without using a  
536 priori determined basis function. The advantage of the EEMD method is that both the frequency  
537 and amplitude of each IMF are determined adaptively from the local characteristic of the time

538 series and they vary as a function of time. The same IMF at all latitudes (here from 35°S to 70°N  
539 with 0.5° resolution) can be pieced together to construct the basin-scale pattern of the AMOC  
540 variability.

541 There are total of nine IMFs for the 60-year monthly mean time series (the first two IMFs represent  
542 the high-frequency intraseasonal variability). The third IMF (Figure 23) represents the variability  
543 of the AMOC transport on seasonal timescale. The results show that the seasonal AMOC  
544 variability is high at all latitudes (Figure 22). It appears at a first glance that the variability is quite  
545 coherent across all latitudes, but there is actually a phase shift that occurs around 15°N. This is  
546 illustrated by the right panel of Figure 23 that displays the mean seasonal variability. The phase in  
547 the subtropical North Atlantic is constant from 15 to 45°N and lags the variability further north in  
548 subpolar North Atlantic. South of 15°N, the phase in the equatorial region leads that of the South  
549 Atlantic Ocean. This phase shift can be seen in observations as well. For example, high seasonal  
550 AMOC transports occur during April-August at 34°S (Figure 10b based on Argo-WOA13 data),  
551 compared to July-November at 26.5°N (Figure 4c based on RAPID data). Most of the AMOC  
552 seasonal variability as well as the phase shift is due to variability in the wind-driven Ekman  
553 transport as discussed by Xu et al. (2014), Zhao and Johns (2014a), and Yang (2015).

554 The fourth and fifth IMFs displayed in Figure 24 represent the interannual variability. Its  
555 magnitude is smaller than that of the seasonal variability, but the phases are relatively constant  
556 across a wide latitudinal range. In order to quantitatively measure the meridional coherence, we  
557 compute the correlation between the interannual variability at a given latitude and the variability  
558 averaged through the whole Atlantic from 35°S to 70°N (see Xu et al., 2019 for an example). The  
559 correlation, shown in Figure 25, is significant from 35°S to 35°N. This result is in good agreement

560 with the findings of Kelly et al. (2014) based on observations and box model, except that their  
561 correlation extends further north to 40°N. As for the seasonal time scale, the interannual variability  
562 of the AMOC is primarily driven by the wind variability (e.g., Roberts et al., 2013; Zhao and  
563 Johns, 2014b).

564 Figure 26 shows the sixth IMF and the sum of the seventh to ninth IMFs, representing the AMOC  
565 variability on decadal and multi-decadal timescales, respectively. The 60-year simulation is too  
566 short to allow for a robust quantification of the multi-decadal variabilities (Figure 26b), but we  
567 find that the variability is consistent with century-long ocean-only simulations performed with  
568 CORE-II (Danabasoglu et al., 2016; Xu et al., 2019). The decadal variability (Figure 26a) is mostly  
569 coherent south of 35°N, as for the interannual variability shown in Figure 25. North of 35°N, there  
570 is sometimes a phase shift with variability of the subpolar North Atlantic leading the variability  
571 further south. This aspect of the decadal variability (i.e., with origin in the subpolar North Atlantic  
572 near 50°N and propagating southward) has been reported previously in several basin scale  
573 simulations (Böning et al. 2006; Xu et al., 2013).

## 574 **6. Summary and Discussion**

575 Through the South Atlantic Ocean, the AMOC is connected to the Indian/Pacific Oceans and is  
576 entangled into the global overturning circulation system. This important region is also particularly  
577 complex, featuring strong boundary currents (jets) and high eddy variability in both the western  
578 and eastern boundaries as well as in the Atlantic sector of the Southern Ocean. Observations of the  
579 full-depth circulation structure are focused on limited places, thus the three-dimensional  
580 circulation structure in the South Atlantic and the large-scale pattern of the AMOC variability are  
581 not well-determined. In this study, we used numerical results from a long-term 1/12° global  
582 simulation, along with observations, to address the fundamental questions regarding the mean

583 circulation pattern in this region as well as the meridional coherence of the AMOC variability. The  
584 model results are shown to represent the transports and the vertical structure of the key circulation  
585 patterns in this region, especially, the AMOC across 34°S in the South Atlantic, the ACC at 65°W  
586 in the Drake Passage, as well as the zonal flows along the PM-GH transect in the open ocean  
587 southwest of Africa. The key results are:

588 1) In the South Atlantic Ocean south of 34°S between the Drake Passage (65°W) and southwest  
589 of Africa (PM-GH), there is a maximum upward transport of 5.6 Sv across 1400 m. The water in  
590 this area undergoes a strong diapycnal transformation: about 12 Sv AAIW and NADW in the  
591 density range of 36.13-37.0 kg/m<sup>3</sup> is transformed toward lighter intermediate water, mostly due to  
592 surface buoyancy forcing.

593 2) In the upper limb of the AMOC, the northward flow originates primarily from the warm Agulhas  
594 leakage. The colder fresher Pacific water also enters the South Atlantic Ocean via eddy motions.  
595 The cold water participates the subtropical gyre and modifies the water properties of the South  
596 Atlantic Ocean; its direct contribution to the northward limb of the AMOC is relatively small (in  
597 the order of 1.5 Sv).

598 3) In the lower limb, the NADW flows southward in the DWBC along the continental slope and  
599 in complex recirculation in the Brazil Basin, especially around the Vitória-Trindade Seamount  
600 Chain near 20°S. The recirculation carries the NADW and its high-salinity signature into the  
601 offshore interior. A weak zonal flow of NADW of ~2 Sv is found to cross the MAR near 22°S.  
602 Different from the schematic of Arhan et al. (2003) based on inverse model and the previous  
603 numerical results of van Sebille et al. (2012), however, this modeled NADW does not continue to  
604 flow eastward across the Angola Basin and southeastward into the Cape Basin. Instead, it turns  
605 northward and circulates around the Angola Basin like the schematic proposed by Hogg and

606 Thurnherr (2005). This NADW circulation pattern is consistent with the water property  
607 distribution, i.e., in both observations and model, the salinity east of MAR is significantly lower  
608 than that to the west. Virtually all of the NADW from the north flows in the DWBC all the way to  
609 40-45°S before turning eastward to flow across the MAR near 42°S. The location of this crossing  
610 can be seen from SSH as a contracted ACC front near 10°W.

611 4) Overall, the modeled AMOC variability from interannual to decadal timescales is meridional  
612 coherent in the Atlantic Ocean from 35°S to about 35°N, in agreement with Kelly et al. (2014).  
613 One may expect a higher degree of meridional coherence in this latitude range because, being  
614 outside of the deep-water formation and/or the upwelling regions, the diapycnal water mass  
615 transformation between the upper and lower AMOC limbs is small and the variability is mostly  
616 wind driven.

617 Although the modeled transport and vertical structure of the South Atlantic presented in this study  
618 are largely consistent with the observations, there is room for improvement. In particular, the  
619 modeled Agulhas rings dissipate too slowly and follow a regular pathway. This leads to a high  
620 EKE tongue that extends much farther to the northwest and impacts the regional circulation pattern  
621 in the eastern South Atlantic. Several remedies have been put forward to improve the realism of  
622 the circulation in the Agulhas region, namely i) using finer horizontal resolution along with a better  
623 representation of the bathymetry features like the Agulhas Bank/Plateau as well as the continental  
624 slope and seamounts (Speich et al., 2006); ii) using a higher order advection scheme which would  
625 lead to more irregularity in Agulhas eddy size and pathway (Backeberg et al., 2009), or iii)  
626 including the ocean current feedback in the wind stress calculation (Renault et al., 2017;  
627 Chassignet et al., 2020). While it is indeed more physical to take into account the vertical shear  
628 between atmospheric winds and ocean currents when computing the wind stress, it does lead to an

629 eddy damping effect that can reduce the kinetic energy by as much as 30% and lead to a serious  
630 underestimation of EKE elsewhere in the domain (Chassignet et al., 2020). There is therefore a  
631 trade-off between a better representation of one current system (the Agulhas) and realistic  
632 energetic and/or variability throughout the globe.

633

634 **Acknowledgement:** The work is supported by NOAA-Earth System Prediction Capability Project  
635 (Award NA15OAR4320064), NOAA Climate Program Office MAPP Program (Award  
636 NA15OAR4310088), and Climate Variability and Predictability Program (Award GC16-210), and  
637 NOAA's Atlantic Oceanographic and Meteorological Laboratory. The numerical simulations were  
638 performed on supercomputers at the Engineer Research and Development Center (ERDC),  
639 Vicksburg, Mississippi, using computer time provided by the U.S. DoD High Performance  
640 Computing Modernization Program. The sea ice extent data are available from National Snow &  
641 Ice data Center (<https://nsidc.org/data>); the altimeter products used here were produced by  
642 Ssalto/Duacs and distributed AVISO, with support from CNES  
643 <http://www.aviso.altimetry.fr/duacs>; the gridded T/S fields from the Argo float measurements are  
644 available at [http://www.argo.ucsd.edu/Gridded\\_fields.html](http://www.argo.ucsd.edu/Gridded_fields.html) and the World Ocean Atlas 2013 is  
645 available at <http://www.nodc.noaa.gov/OC5/woa13>; the velocity at 1000 m is obtained from  
646 <http://apdrc.soest.hawaii.edu/projects/Argo/data/trjctry>; the global model outputs are stored in the  
647 ERDC archive server and the model results presented in this study are available in HYCOM server  
648 (<ftp://ftp.hycom.org/pub/xbxu/GLBb0.08/SATL>).

649

650 **Reference:**

- 651 Arhan, M., Mercier H., & Park Y.-H. (2003). On the deep water circulation of the eastern South Atlantic  
652 Ocean. *Deep-Sea Research Part I*, **50**, 889–916, [https://doi.org/10.1016/S0967-0637\(03\)00072-4](https://doi.org/10.1016/S0967-0637(03)00072-4)
- 653 Backeberg, B. C., Bertino, L., & Johannessen, J. A. (2009). Evaluating two numerical advection schemes  
654 in HYCOM for eddy-resolving modelling of the Agulhas Current, *Ocean Science*, **5**, 173-190,  
655 <https://doi.org/10.5194/os-5-173-2009>
- 656 Baringer, O. M., & Garzoli, S. L. (2007). Meridional heat transport determined with expendable  
657 bathythermographs. Part I: Error estimates from model and hydrographic data. *Deep-Sea Research Part*  
658 *I*, **54**, 1390–1401, <https://doi.org/10.1016/j.dsr.2007.03.011>
- 659 Beal, L. M., De Ruijter, W. P. M., Biastoch, A., Zahn, R., & SCOR/WCRP/IAPSO Working Group 136  
660 (2011). On the role of the Agulhas system in ocean circulation and climate, *Nature*, **472** (7344), 429–  
661 436, <https://doi.org/10.1038/nature09983>
- 662 Bleck, R. (2002). An oceanic general circulation model framed in hybrid isopycnic-Cartesian coordinates.  
663 *Ocean Modelling*, **37**, 55–88.
- 664 Böning, C. W., Scheinert, M., Dengg, J., Biastoch, A., & Funk, A. (2006). Decadal variability of subpolar  
665 gyre transport and its reverberation in the North Atlantic overturning, *Geophys. Res. Lett.*, **33**, L21S01,  
666 <https://doi.org/10.1029/2006GL026906>.
- 667 Bower, A., Lozier, S., Biastoch, A., Drouin, K., Foukal, N., Furey, H., et al. (2019). Lagrangian views of  
668 the pathways of the Atlantic Meridional Overturning Circulation. *Journal of Geophysical Research:*  
669 *Oceans*, **124** (8), 5313-5335. <https://doi.org/10.1029/2019JC015014>
- 670 Brambilla, E., Talley, L. D. & Robbins, P. E. (2008). Subpolar Mode Water in the northeastern Atlantic: 2.  
671 Origin and transformation. *Journal of Geophysical Research: Oceans*, **113**(C4). <https://doi.org/10.1029/2006JC004063>
- 672
- 673 Broecker, W. S. (1991). The great ocean conveyor, *Oceanography*, **4** (2):79–89.
- 674 Carnes, M. R. (2009). Description and evaluation of GDEM-V3.0. Tech. Rep. NRL/MR/7330–09–9165,  
675 21 pp., Naval Research Laboratory, Stennis Space Center, Miss.
- 676 Chassignet, E. P., Smith, L. T., Halliwell, G. R. & Bleck, R. (2003). North Atlantic simulations with the  
677 hybrid coordinate ocean model (HYCOM): Impact of the vertical coordinate choice, reference pressure,  
678 and thermobaricity, *Journal of Physical Oceanography*, **33** (12), 2504–2526.
- 679 Chassignet, E. P., Hurlburt, H. E., Smedstad, O. M., Halliwell, G. R., Wallcraft, A. J., Metzger, E. J., et al.  
680 (2006). Generalized vertical coordinates for eddy-resolving global and coastal ocean forecasts,  
681 *Oceanography*, **19** (1), 20–31. <https://doi.org/10.5670/oceanog.2006.95>
- 682 Chassignet, E. P., Yeager, S. G., Fox-Kemper, B., Bozec, A., Castruccio, F., Danabasoglu, G. et al. (2020).  
683 Impact of horizontal resolution on global ocean-sea-ice model simulations based on the experimental  
684 protocols of the Ocean Model Intercomparison Project phase 2 (OMIP-2), *Geoscientific Model*  
685 *Development*, <https://doi.org/10.5194/gmd-2019-374-RC2>
- 686 Chidichimo, M. P., Donohue, K. A., Watts, D. R., & Tracey, K. L. (2014). Baroclinic transport time series  
687 of the Antarctic Circumpolar Current measured in Drake Passage, *Journal of Physical Oceanography*,  
688 **44** (7), 1829–1853. <https://doi.org/10.1175/JPO-D-13-071.1>
- 689 Colin de Verdière, A., & Ollitrault, M. (2016). A direct determination of the World Ocean barotropic  
690 circulation, *Journal of Physical Oceanography*, **46**, 255-273, <https://doi.org/10.1175/JPO-D-15-0046.1>.
- 691 Cunningham, S. A., Alderson, S. G., King, B. A., & Brandon M. A. (2003). Transport and variability of the  
692 Antarctic Circumpolar Current in Drake Passage, *Journal of Geophysical Research-Oceans*, **108** (C5),  
693 8084, <https://doi.org/10.1029/2001JC001147>.

- 694 Delandmeter, P., & van Sebille, E. (2019). The Parcels v2.0 Lagrangian framework: new field interpolation  
695 schemes, *Geoscientific Model Development*, **12**, 3571–3584, <https://doi.org/10.5194/gmd-12-3571->  
696 2019.
- 697 Dong, S., Garzoli, S., Baringer, M., Meinen, C., & Goni, G. (2009). Interannual variations in the Atlantic  
698 meridional overturning circulation and its relationship with the net northward heat transport in the South  
699 Atlantic. *Geophysical Research Letter*, **36**, L20606, <https://doi.org/10.1029/2009GL039356>.
- 700 Dong, S., Garzoli, S., & Baringer, M. (2011). The Role of inter-ocean exchanges on decadal variations of  
701 the meridional heat transport in the South Atlantic. *Journal of Physical Oceanography*, **41**, 1498–1511.  
702 <https://doi.org/10.1175/2011JPO4549.1>.
- 703 Dong, S., Baringer, M. O., Goni, G. J. Meinen, C. S., & Garzoli, S. L. (2014). Seasonal variations in the  
704 South Atlantic meridional overturning circulation from observations and numerical models,  
705 *Geophysical Research Letter*, **41**, 4611–4618, <https://doi.org/10.1002/2014GL060428>.
- 706 Dong, S., Goni, G., & Bringas, F. (2015). Temporal variability of the South Atlantic Meridional  
707 Overturning Circulation between 20°S and 35°S, *Geophysical Research Letter*, **42**, 7655–7662,  
708 <https://doi.org/10.1002/2015GL065603>.
- 709 Donners, J., & Drijfhout, S. S. (2004). The Lagrangian view of South Atlantic interocean exchange in a  
710 global ocean model compared with inverse model results, *Journal of Physical Oceanography*, **34** (5),  
711 1019–1035.
- 712 Donohue, K. A., Tracey, K. L., Watts, D. R., Chidichimo, M. P., & Chereskin, T. K. (2016). Mean Antarctic  
713 Circumpolar Current transport measured in Drake Passage. *Geophysical Research Letters*, **43**, 11760–  
714 11767. <https://doi.org/10.1002/2016GL070319>.
- 715 Fetterer, F., Knowles, K., Meier, W., Savoie, M., & Windnagel, A. K. (2017). Sea Ice Index, Version 3.  
716 Boulder, Colorado USA. NSIDC: National Snow and Ice Data Center.  
717 <http://dx.doi.org/10.7265/N5K072F8>.
- 718 Firing, Y. L., Chereskin, T. K., & Mazloff, M. R. (2011). Vertical structure and transport of the Antarctic  
719 Circumpolar Current in Drake Passage from direct velocity observations, *Journal of Geophysical*  
720 *Research-Oceans*, **116**, <https://doi.org/10.1029/2011JC006999>.
- 721 Friocourt, Y., Drijfhout, S., Blanke, B., & Speich, S. (2005). Water mass export from Drake Passage to the  
722 Atlantic, Indian, and Pacific Oceans: A Lagrangian model analysis. *Journal of Physical Oceanography*,  
723 **35** (7), 1206–1222. <https://doi.org/10.1175/JPO2748.1>
- 724 Garzoli, S. L., & Matano, R. (2011). The South Atlantic and the Atlantic Meridional Overturning  
725 Circulation, *Deep-Sea Research Part II*, **58** (17-18), 1837–1847,  
726 <https://doi.org/10.1016/j.dsr2.2010.10.063>.
- 727 Garzoli, S. L., Baringer, M. O., Dong, S., Perez, R. C., & Yao, Q. (2013). South Atlantic meridional fluxes,  
728 *Deep-Sea Research Part I*, **71**, 21–32, <https://doi.org/10.1016/j.dsr.2012.09.003>.
- 729 Garzoli, S. L., Dong, S., Fine, R., Meinen, C. S., Perez, R. C., Schmid, C., et al. (2015). The fate of the  
730 Deep Western Boundary Current in the South Atlantic, *Deep-Sea Research Part I*, **103**, 125–136,  
731 <https://doi.org/10.1016/j.dsr.2015.05.008>.
- 732 Gladyshev, S., Arhan, M., Sokov, A., & Speich S. (2008). A hydrographic section from South Africa to  
733 the southern limit of the Antarctic Circumpolar Current at the Greenwich meridian, *Deep-Sea Research*  
734 *Part I*, **55**, 1284–1303, <https://doi.org/10.1016/j.dsr.2008.05.009>.
- 735 Goes, M., Goni, G. & Dong, S. (2015). An optimal XBT-based monitoring system for the South Atlantic  
736 meridional overturning circulation at 34S, *Journal of Geophysical Research-Oceans*, **120**, 161–181,  
737 <https://doi.org/10.1002/2014JC010202>.

- 738 Gordon, A. L. (1986). Interocean exchange of thermocline water, *Journal of Geophysical Research-*  
 739 *Oceans*, **91** (C4), 5037–5046, <https://doi.org/10.1029/JC091iC04p05037>.
- 740 Gordon, A.L. (2001). Interocean Exchange. in *Ocean Circulation and Climate*, G. Siedler, J. Church, and  
 741 J. Gould, eds. Academic Press. Chapter 4.7, 303–314.
- 742 Hogg, N. G., & Owens, W. B. (1999). Direct measurement of the deep circulation within the Brazil Basin.  
 743 *Deep-Sea Research Part II*. **46**, 335–353, <http://dx.doi.org/10.1029/2004/JC002311>.
- 744 Hogg, N. G., & Thurnherr, A. M. (2005). A zonal pathway for NADW in the South Atlantic. *Journal of*  
 745 *Oceanography*. **61**(3), 493–507, <https://doi.org/10.1007/s10872-005-0058-7>.
- 746 Hogg, N. G., Biscaye, P. E., Gardner, W. D., & Schmitz, W. J. Jr. (1982). On the Transport and Modification  
 747 of Antarctic Bottom Water in the Vema Channel, *Journal of Marine Research*, **40**, 231-263.
- 748 Hunke, E. C., & Lipscomb, W. H. (2008). CICE: The Los Alamos sea ice model documentation and  
 749 software user’s manual, version 4.0, Tech. Rep. LA-CC-06-012, Los Alamos Natl. Lab., Los Alamos,  
 750 N. M.
- 751 Kelly, K. A., Thompson, L., & Lyman, J. (2014). The coherence and impact of meridional heat transport  
 752 anomalies in the Atlantic Ocean inferred from observations, *Journal of Climate*, **27**, 1469–1487,  
 753 <https://doi.org/10.1175/JCLI-D-12-00131.1>.
- 754 Kim, Y. S., & Orsi, A. H. (2014). On the variability of Antarctic Circumpolar Current fronts inferred from  
 755 1992–2011 altimetry, *Journal of Physical Oceanography*, **44** (12), 3054–3071,  
 756 <https://doi.org/10.1175/JPO-D-13-0217.1>.
- 757 Klatt, O., Fahrbach, E., Hoppeman, M. & Rohardt, G. (2005). The transport of the Weddell Gyre across the  
 758 prime meridian, *Deep-Sea Research Part II*, **52**, 513–528. <https://doi.org/10.1016/j.dsr2.2004.12.015>.
- 759 Kersalé, M., Perez, R. C., Speich, S., Meinen, C. S., Lamont, T., Le Hénaff, M., et al. (2019). Shallow and  
 760 Deep Eastern Boundary Currents in the South Atlantic at 34.5°S: Mean structure and variability, *Journal*  
 761 *of Geophysical Research-Oceans*, <https://doi.org/10.1029/2018JC014554>.
- 762 Koenig Z., Provost, C., Ferrari, R., Sennéchael, N., & Rio, M.-H. (2014). Volume transport of the Antarctic  
 763 Circumpolar Current: Production and validation of a 20 year long times series obtained from in situ and  
 764 satellite data, *Journal of Geophysical Research-Oceans*, **119**, 5407–5433,  
 765 <https://doi.org/10.1002/2014JC009966>.
- 766 Koenig, Z., Provost, C., Park, Y.-H., Ferrari, R., & Sennéchael, N. (2016). Anatomy of the Antarctic  
 767 Circumpolar Current volume transports through Drake Passage, *Journal of Geophysical Research-*  
 768 *Oceans*, **121**, 2572–2595, <https://doi.org/10.1002/2015JC011436>.
- 769 Koltermann, K.P., Gouretski, V.V. & Jancke, K. (2011). Hydrographic Atlas of the World Ocean  
 770 Circulation Experiment (WOCE). Volume 3: Atlantic Ocean (eds. M. Sparrow, P. Chapman and J.  
 771 Gould). International WOCE Project Office, Southampton, UK, ISBN 090417557X.
- 772 Langehaug, H. R., Rhines, P. B., Eldevik, T., Mignot, J., & Lohmann, K. (2012). Water mass transformation  
 773 and the North Atlantic Current in three multicentury climate model simulations. *Journal of Geophysical*  
 774 *Research-Oceans*, **117** (C11), <https://doi.org/10.1029/2012JC008021>.
- 775 Large, W. G., & Yeager, S. (2004). Diurnal to decadal global forcing for ocean and sea-ice models: The  
 776 data sets and flux climatologies. NCAR Tech. Note NCAR/TN 460+STR.
- 777 Legeais, J. F., Speich, S., Arhan, M., Ansrorge, I. J., Fahrbach, E., Garzoli, S., & Klepikov, A. (2005). The  
 778 baroclinic transport of the Antarctic Circumpolar Current south of Africa, *Geophysical Research Letter*,  
 779 **32**, L24602, <https://doi.org/10.1029/2005GL023271>.

- 780 Locarnini, R. A., Mishonov, A. V., Antonov, J. I., Boyer, T. P., Garcia, H. E., Baranova, O. K., et al. (2013).  
781 Temperature. Vol. 1, World Ocean Atlas 2013, S. Levitus, Ed., A. Mishonov Technical Ed., NOAA  
782 Atlas NESDIS 73, 40 pp.
- 783 Loeb, N. G., Lyman, J. M., Johnson, G. C. Allan, R. P., Doelling, D. R., Wong, T., et al. (2012). Observed  
784 changes in top-of-the-atmosphere radiation and upper-ocean heating consistent within uncertainty,  
785 *Nature Geoscience*, **5**, 110–113, doi:10.1038/NGEO1375.
- 786 Macdonald, A. M., & Baringer, M. O. (2013). Ocean heat transport. In *Ocean Circulation and Climate: A*  
787 *21st Century Perspective*, G. Siedler et al., Eds., International Geophysics Series, **103**, Academic Press,  
788 759–786, <https://doi.org/10.1016/B978-0-12-391851-2.00029-5>.
- 789 Maltrud, E.M., & McClean, J. (2005). An Eddy Resolving Global 1/10° Ocean Simulation, *Ocean*  
790 *Modelling*, **8**, 31-54, <http://dx.doi.org/10.1016/j.ocemod.2003.12.001>.
- 791 Meinen, C. S., Piola, A. R., Perez, R. C., & Garzoli, S. L. (2012). Deep Western Boundary Current transport  
792 variability in the South Atlantic: preliminary results from a pilot array at 34.5°S, *Ocean Science*, **8**,  
793 1041–1054, <https://doi.org/10.5194/os-8-1041-2012>.
- 794 Meinen, C. S., Speich, S., Perez, R. C., Dong, S., Piola, A. R., Garzoli, S. L., et al. (2013). Temporal  
795 variability of the Meridional Overturning Circulation at 34.5°S: Results from two pilot boundary arrays  
796 in the South Atlantic, *Journal of Geophysical Research-Oceans*, **118**, 6461–6478,  
797 <https://doi.org/10.1002/2013JC009228>.
- 798 Meinen, C. S., Garzoli, S. L., Perez, R. C., Campos, E., Piola, A. R., Chidichimo, M. P., et al. (2017).  
799 Characteristics and causes of Deep Western Boundary Current transport variability at 34.5°S during  
800 2009–2014, *Ocean Science*, **13**, 175-194, <https://doi.org/10.5194/os-13-175-2017>.
- 801 Meinen, C. S., Speich, S., Piola, A. R., Ansorge, I., Campos, E., Kersalé, M., et al. (2018). Meridional  
802 Overturning Circulation transport variability at 34.5°S during 2009–2017: Baroclinic and barotropic  
803 flows and the dueling influence of the boundaries, *Geophysical Research Letter*, **45**, 4180–4188,  
804 <https://doi.org/10.1029/2018GL077408>.
- 805 Meredith, M. P., Woodworth, P. L., Chereskin, T. K., Marshall, D. P., Allison, L. C., Bigg, G. R., et al.  
806 (2011). Sustained monitoring of the Southern Ocean at Drake Passage: Past achievements and future  
807 priorities. *Reviews of Geophysics*, **49**, RG4005. <https://doi.org/10.1029/2010RG000348>.
- 808 Mulet, S., Rio, M. H., Etienne, H., Artana, C., Cancet, M., Dibarboure, G., et al. (2020). The new CNES-  
809 CLS18 Global Mean Dynamic Topography, Submitted to *Ocean Science*.
- 810 Orsi, A. H., Whitworth, T. III, & Nowlin, W. D. Jr. (1995). On the meridional extent and fronts of the  
811 Antarctic Circumpolar Current, *Deep-Sea Research Part I*, **42**, 641–673.
- 812 Renault, L., McWilliams, J. C., & Penven, P. (2017). Modulation of the Agulhas Current retroflexion and  
813 leakage by oceanic current interaction with the atmosphere in coupled simulations, *Journal Physical*  
814 *Oceanography*, **47**, 2077–2100, <https://doi.org/10.1175/JPOD-16-0168.1>.
- 815 Richardson, P. L. (2007). Agulhas leakage into the Atlantic estimated with subsurface floats and surface  
816 drifters, *Deep-Sea Research Part I*, **54**, 1361–1389, <https://doi.org/10.1016/j.dsr.2007.04.010>.
- 817 Richardson, P. L. (2008). On the history of meridional overturning circulation schematic diagrams.  
818 *Progress in Oceanography*, **76**, 466-486, <https://doi.org/10.1016/j.pocean.2008.01.005>.
- 819 Rintoul, S. R. (1991). South Atlantic interbasin exchange, *Journal of Geophysical Research-Oceans*, **96**  
820 (C2), 2675–2692, <https://doi.org/10.1029/90JC02422>.
- 821 Roberts, C. D., Waters, J., Peterson, K. A., Palmer, M. D., McCarthy, G. D., Frajka-Williams, E., et al.  
822 (2013). Atmosphere drives recent interannual variability of the Atlantic meridional overturning  
823 circulation at 26.5°N, *Geophysical Research Letters*, **40**, 5164–5170, <https://doi.org/10.1002/grl.50930>.

- 824 Roemmich, D., Church, J., Gilson, J., Monselesan, D., Sutton, P., & Wijffels, S. (2015). Unabated planetary  
 825 warming and its ocean structure since 2006. *Nature Climate Change*, **5**, 240-245,  
 826 <https://doi.org/10.1038/nclimate2514>.
- 827 Rodrigues, R. R., Wimbush, M., Watts, D. R., Rothstein, L. M., & Ollitrault, M. (2010). South Atlantic  
 828 mass transports obtained from subsurface float and hydrographic data. *Journal of Marine Research*, **68**,  
 829 819– 850, <https://doi.org/10.1357/002224010796673858>.
- 830 Rousselet, L., Cessi, P., & Forget, G. (2020). Routes of the upper branch of the Atlantic meridional  
 831 overturning circulation according to an ocean state estimate, *Geophysical Research Letters*,  
 832 <https://doi.org/10.1029/2020GL089137>.
- 833 Rühls, S., Schwarzkopf, F. U., Speich, S., & Biastoch, A. (2019). Cold vs. warm water route—Sources for  
 834 the upper limb of the Atlantic meridional overturning circulation revisited in a high-resolution ocean  
 835 model, *Ocean Science*, **15**, 489–512.
- 836 Sallée, J.-B., Speer, K., & Morrow, R. (2008). Response of the Antarctic Circumpolar Current to  
 837 atmospheric variability, *Journal of Climate*, **21** (12), 3020–30391,  
 838 <https://doi.org/10.1175/2007JCLI1702.1>.
- 839 Saracerno, M., Provost, C., & Zajaczkovski, U. (2009). Long-term variation in the anticyclonic ocean  
 840 circulation over Zapiola Rise as observed by satellite altimetry: Evidence of possible collapses, *Deep-*  
 841 *Sea Research Part I*, **56**, 1077-1092, <https://doi.org/10.1016/j.dsr.2009.03.005>.
- 842 Saunders, P. M., & King, B. A. (1995). Oceanic fluxes on the WOCE A11 section, *Journal of Physical*  
 843 *Oceanography*, **25**, 1942–1958.
- 844 Schlitzer, R. (1996). Mass and Heat Transports in the South Atlantic Derived from Historical Hydrographic  
 845 Data, in *The South Atlantic*. Springer, Berlin, Heidelberg
- 846 Schmitz, W. J. Jr. (1995). On the interbasin-scale thermohaline circulation, *Reviews of Geophysics*, **33** (2),  
 847 151–173, <https://doi.org/10.1029/95RG00879>.
- 848 Schmitz, W. J. Jr. (1996). On the World Ocean Circulation: Volume I. Technical Report, WHOI-96-03.  
 849 140 pp.
- 850 Smeed, D. A., Josey, S. A., Beaulieu, C., Johns, W. E., Moat, B. I., Frajka-Williams, E., et al. (2018). The  
 851 North Atlantic Ocean is in a state of reduced overturning, *Geophysical Research Letters*, **45**, 1527–  
 852 1533, <https://doi.org/10.1002/2017GL076350>.
- 853 Sokolov, S., & Rintoul, S. R. (2009). Circumpolar structure and distribution of the Antarctic Circumpolar  
 854 Current fronts: 1. Mean circumpolar paths, *Journal of Geophysical Research*, **114**, C11018,  
 855 <https://doi.org/10.1029/2008JC005108>.
- 856 Speer, K. & Tziperman, E. (1992). Rates of water mass formation in the North Atlantic Ocean, *Journal of*  
 857 *Physical Oceanography*, **22**(1), 93-104.
- 858 Speer, K. G., Siedler, G. & Talley, L. (1995). The Namib Col Current, *Deep-Sea Research Part I*, **42**, 1933–  
 859 1950.
- 860 Speer, K. G. & Zenk, W. (1993). The flow of Antarctic Bottom Water into the Brazil Basin, *Journal of*  
 861 *Physical Oceanography*, **23**, 2667-2682.
- 862 Speich, S., Blanke, B., & Madec, G. (2001). Warm and cold water routes of an OGCM thermohaline  
 863 conveyor belt, *Geophysical Research Letters*, **28**, 311–314.
- 864 Speich, S., Lutjeharms, J. R. E., Penven, P., & Blanke, B. (2006). Role of bathymetry in Agulhas Current  
 865 configuration and behaviour, *Geophysical Research Letters*, **33**, L23611, doi:10.1029/2006GL027157.
- 866 Stramma, L., & England, M. (1999). On the water masses and mean circulation of the South Atlantic Ocean,  
 867 *Journal of Geophysical Research*, **104**, 20,863–20,883, <https://doi.org/10.1029/1999JC900139>.

- 868 Swart, S., Speich, S., Ansorge, I. J., Goni, G. J., Gladyshev, S. & Lutjeharms, J. R. E. (2008). Transport  
869 and variability of the Antarctic Circumpolar Current south of Africa, *Journal of Geophysical Research-*  
870 *Oceans*, **113**, C09014, <https://doi.org/10.1029/2007JC004223>.
- 871 Talley, L. D. (2013). Closure of the Global Overturning Circulation Through the Indian, Pacific, and  
872 Southern Oceans: Schematics and Transports. *Oceanography*, **26** (1), 80–97,  
873 <https://doi.org/10.5670/oceanog.2013.07>.
- 874 Trenberth, K. E., Zhang, Y., Fasullo, J. T. & Cheng, L. (2019). Observation-based estimates of global and  
875 basin ocean meridional heat transport time series, *Journal of Climate*, 4567–4583,  
876 <https://doi.org/10.1175/JCLI-D-18-0872.1>.
- 877 Tsujino H., Urakawa, S., Nakano, H., Small, R. J., Kim, W. M., Yeager, S. G. et al. (2018). JRA-55 based  
878 surface dataset for driving ocean-sea-ice models (JRA55-do), *Ocean Modelling*, **130**, 79–139,  
879 <https://doi.org/10.1016/j.ocemod.2018.07.002>.
- 880 van Sebille, E., Johns, W. E., & Beal, L. M. (2012). Does the vorticity flux from Agulhas rings control the  
881 zonal pathway of NADW across the South Atlantic? *Journal of Geophysical Research: Oceans*, **117**,  
882 C05037, <https://doi.org/10.1029/2011JC007684>.
- 883 Walin, G. (1982). On the relation between sea-surface heat flow and thermal circulation in the ocean,  
884 *Tellus*, **34** (2), 187–195.
- 885 Warren, B. A. & Speer, K. G. (1991). Deep circulation in the eastern South Atlantic Ocean, *Deep-Sea*  
886 *Research Part I*, **38** (1991), S281–S322.
- 887 Whitworth, T. III (1983). Monitoring the transport of the Antarctic Circumpolar Current at Drake Passage,  
888 *Journal of Physical Oceanography*, **13**, 2045–2057.
- 889 Whitworth, T., III, & Peterson R. G. (1985). Volume transport of the Antarctic Circumpolar Current from  
890 bottom pressure measurements, *Journal of Physical Oceanography*, **15**, 810–816.
- 891 Whitworth, T., & Nowlin, W. D. (1987). Water masses and currents of the Southern Ocean at the  
892 Greenwich meridian, *Journal of Geophysical Research*, **92** (C6), 6462–6476.
- 893 Wu, Z., & Huang, N. E. (2009). Ensemble empirical mode decomposition: A noise-assisted data analysis  
894 method, *Advances in Adaptive Data Analysis*, **1** (1), 1–41, <https://doi.org/10.1142/S1793536909000047>
- 895 Xu, X., Hurlburt, H. E., Schmitz, W. J. Jr., Fischer, J., Zantopp, R., & Hogan, P. J. (2013). On the currents  
896 and transports connected with the Atlantic meridional overturning circulation in the subpolar North  
897 Atlantic, *Journal of Geophysical Research: Oceans*, **118**, doi:10.1002/jgrc.20065.
- 898 Xu, X., Chassignet, E. P., Johns, W. E., Schmitz W. J. Jr., & Metzger, E. J. (2014). Intraseasonal to  
899 interannual variability of the Atlantic meridional overturning circulation from eddy-resolving  
900 simulations and observations. *Journal of Geophysical Research: Oceans*, **119**, 5140–5159,  
901 <https://doi.org/10.1002/2014JC009994>.
- 902 Xu, X., Rhines, P. B., & Chassignet, E. P. (2018). On mapping the diapycnal water mass transformation of  
903 the upper North Atlantic Ocean, *Journal of Physical Oceanography*, **48**, 2233–2258,  
904 <https://doi.org/10.1175/JPO-D-17-0223.1>.
- 905 Xu, X., Chassignet, E. P., & Wang, F. (2019). On the variability of the Atlantic meridional overturning  
906 circulation transports in coupled CMIP5 simulations, *Climate Dynamics*,  
907 <https://doi.org/10.1007/s00382-018-4529-0>.
- 908 Xu, X., Chassignet, E. P., Firing, Y. L., & Donohue, K. (2020). Antarctic Circumpolar Current transport  
909 through Drake Passage: What can we learn from comparing high-resolution model results to  
910 observations? *Journal of Geophysical Research: Oceans*, **125**, e2020JC016365,  
911 <https://doi.org/10.1029/2020JC016365>.

- 912 Yang, J. (2015). Local and remote wind-stress forcing of the seasonal variability of the Atlantic Meridional  
913 Overturning Circulation (AMOC) transport at 26.5°N. *Journal of Geophysical Research: Oceans*, **120**,  
914 doi:10.1002/2014JC010317.
- 915 Zhang, R. (2010). Latitudinal dependence of Atlantic meridional overturning circulation (AMOC)  
916 variations, *Geophysical Research Letter*, **37**, L16703, <https://doi.org/10.1029/2010GL044474>.
- 917 Zhao, J., & Johns, W. E. (2014a). Wind driven seasonal cycle of the Atlantic meridional overturning  
918 circulation, *Journal of Physical Oceanography*, **44** (6), 1541–1562, doi:10.1175/JPO-D-13-0144.1.
- 919 Zhao, J., & Johns, W. E. (2014b). Wind-forced interannual variability of the Atlantic meridional  
920 overturning circulation at 26.5°N, *Journal of Geophysical Research: Oceans*, **119**, 2403–2419,  
921 doi:10.1002/2013JC009407.
- 922 Zweng, M. M., Reagan, J. R., Antonov, J. I., Locarnini, R. A., Mishonov, A.V., Boyer, T.P., et al. (2013).  
923 Salinity. Vol. 2, World Ocean Atlas 2013, S. Levitus, Ed., A. Mishonov Technical Ed.; NOAA Atlas  
924 NESDIS 74, 39 pp.
- 925

926 **Figure Caption**

927  
928 Figure 1: Model bathymetry (in km) along with key topographic features in the South Atlantic Ocean. Red  
929 lines denote three sections where significant observations have been obtained and the observations are used  
930 to evaluate the model results: 34°S in the South Atlantic, 65°W in Drake Passage, and the Prime Meridian-  
931 Good Hope (PM-GH) transect southwest of Africa.

932  
933 Figure 2: Time evolution of global domain-averaged a) potential temperature in °C and b) total kinetic  
934 energy in  $\text{cm}^2\text{s}^{-2}$  from the global ocean-sea ice simulation. Thin and thick lines denote monthly and annual  
935 means, respectively.

936  
937 Figure 3: Time evolution of a) monthly mean sea ice extent and b) annual mean sea ice extent anomaly  
938 relative to the 1980-2015 average. The sea ice extent is defined as the area (in  $10^6 \text{ km}^2$ ) with sea ice  
939 concentration of 15% or higher. The red/blue lines are model results in the northern/ southern hemisphere;  
940 black lines are observations from National Snow and Ice Data Center.

941  
942 Figure 4. a) Time evolution of the modeled monthly mean transport of the Atlantic meridional overturning  
943 circulation (AMOC) at 26.5°N; thick line denotes a 10-year averages; b) Variability of the modeled AMOC  
944 transports (red line), the observed AMOC transports (black line) from the RAPID array (e.g., Smeed et al.,  
945 2018), and the observed meridional heat transport (MHT, blue line) from Trenberth et al. (2019), all in 12-  
946 month moving average; c) Seasonal variability of the AMOC transports at 26.56°N averaged over 2004-  
947 2017 from model (red line) and the RAPID array (black line).

948  
949 Figure 5. Observed and modeled distributions of a-b) time mean sea surface height (SSH, in cm), c-d) SSH  
950 standard deviation (in cm), and e-f) eddy kinetic energy (EKE, in  $\text{cm}^2 \text{ s}^{-2}$ ) of the surface current in the  
951 southern Atlantic. In observation, the mean SSH is based on long-term climatology CNES-CLS18 (Rio et  
952 al., 2019); the SSH standard deviation and EKE are based on AVISO data in 1993-2018. All model results  
953 are also in 1993-2018.

954  
955 Figure 6: Observed and modeled sea-surface height (SSH) anomaly along the Prime Meridian in latitude  
956 range 20-40°S from 1993 to 2018. The high SSH anomaly denotes the west-/northwestward translation of  
957 the Agulhas Rings that pass the Prime Meridian.

958  
959 Figure 7. a-d) Potential temperature  $\theta$  and salinity  $S$  distributions across 34°S. Observations are based on a  
960 combination of Argo profiles for the top 2000 m and World Ocean Atlas 2013 (WOA13) below 2000 m;  
961 model results are from the global 1/12° HYCOM simulation. Three red lines denote isopycnic surfaces ( $\sigma_2$   
962 of 35.65, 36.58, and 37.12  $\text{kg m}^{-3}$ ) that divide the water column into near surface water, Antarctic  
963 Intermediate Water (AAIW), North Atlantic Deep Water (NADW), and Antarctic Bottom Water (AABW).  
964 e-f) Volumetric  $\theta$ - $S$  diagram along 34°S. Color shading shows the volume percentage for water mass with  
965  $\Delta\theta$ ,  $\Delta S$  resolution of 0.1°C, 0.02 psu (percentages for near surface water, AAIW, NADW and AABW are  
966 also listed); circled lines are volume-weighted  $\theta$ - $S$  profile in observations (black) and model results (red).

967  
968 Figure 8. Observed and modeled time mean meridional velocity across 34°S and the corresponding volume  
969 transport for the four density layers: near surface water ( $\sigma_2 < 35.65 \text{ kg m}^{-3}$ ), Antarctic Intermediate Water  
970 (AAIW,  $35.65 < \sigma_2 < 36.58$ ), North Atlantic Deep Water (NADW,  $36.58 < \sigma_2 < 37.12$ ), and Antarctic Bottom  
971 Water (AABW,  $\sigma_2 > 37.12$ ). Observations are based on a combination of Argo-WOA13 profiles; model  
972 results based on the global 1/12° HYCOM simulation.

973

974 Figure 9. Long-term mean meridional overturning streamfunction (in Sv) at 34°S with respect to a) depth  
 975 and b) potential density in  $\sigma_2$ . Observations based on monthly mean Argo-WOA13 profiles; model results  
 976 based a global 1/12° HYCOM simulation (1979-2018).

977  
 978 Figure 10: a) Time series of the AMOC transport variability (in Sv) at 34°S based on Argo-WOA13 (black,  
 979 Dong et al., 2014), SAMOC-mooring array (blue, Meinen et al., 2018), and global HYCOM (red). The thin  
 980 and thick lines represent monthly means and 12-month moving averages, respectively. b) AMOC transport  
 981 variability at seasonal timescale, with each dot representing the multi-year average of the monthly AMOC  
 982 transport.

983  
 984 Figure 11: Modeled long-term mean zonal velocity and the corresponding four-layer volume transport in  
 985 four density layers across a) 65°W in the Drake Passage and b) the Prime Meridian-Good Hope (PM-GH)  
 986 transect southwest of Africa. The triangles denote the locations of Antarctic circumpolar current (ACC)  
 987 fronts, from south to north, the Southern Boundary, South ACC Front, Polar Front, Subantarctic Front, and  
 988 the subtropical front in panel b. The shaded area in panel b) between 40 and 55.5°S marks the ACC regime  
 989 across the PM-GH transect. Transport is accumulative northward. The four layers are near surface water  
 990 ( $\sigma_2 < 35.65 \text{ kg m}^{-3}$ ), Antarctic Intermediate Water (AAIW,  $35.65 < \sigma_2 < 36.58$ ), North Atlantic Deep Water  
 991 (NADW,  $36.58 < \sigma_2 < 37.12$ ), and Antarctic Bottom Water (AABW,  $\sigma_2 > 37.12$ ).

992  
 993 Figure 12: a) Variability of the modeled ACC transport through the Drake Passage at the 65°W, with thin  
 994 and thick lines represent monthly means and annual means, respectively; b) Seasonal variability of the  
 995 modeled ACC transports averaged over 1979-2018.

996  
 997 Figure 13: a) Modeled mean horizontal transports (Sv per 100m) in the vertical across the 34°S, the 65°W,  
 998 and the PM-GH transects; b) The net transports into the region enclosed by the three transects, with positive  
 999 (negative) values indicating net transport into (out of) the region.

1000  
 1001 Figure 14: a) Net transports into the South Atlantic region enclosed by the 34°S, the 65°W, and the PM-  
 1002 GH transects, with respect to density layers (positive/negative values for net transport into/out of the  
 1003 region); b) Solid line denotes the total diapycnal transformation; dashed line denotes the diapycnal  
 1004 transformation calculated from surface buoyancy fluxes.

1005  
 1006 Figure 15: Modeled long-term mean horizontal transport streamfunction (in Sv) for the layer of near surface  
 1007 water ( $\sigma_2 < 35.65 \text{ kg m}^{-3}$ ). Red and pink streamlines (increment of 1 Sv) denote AMOC contribution and  
 1008 ACC flow; orange streamlines (increment of 2 Sv) denote the subtropical gyre of the South Atlantic.

1009  
 1010 Figure 16: Modeled long-term mean horizontal transport streamfunction (Sv) for the layer of AAIW  
 1011 ( $35.65 < \sigma_2 < 36.58 \text{ kg m}^{-3}$ ). Pink streamlines (increment of 4 Sv) is the ACC; red and orange streamlines  
 1012 denote AMOC contribution and the subtropical gyre of the South Atlantic (similar to Figure 15). The dashed  
 1013 blue lines denote 34°S, 45°S, and the GoodHope sections, across which the water properties of the  
 1014 northward and northwestward transports are examined in Figure 17.

1015  
 1016 Figure 17: Modeled northward transports projected on potential temperature-salinity ( $\theta$ -S) plane across 6  
 1017 sections; the transport presented in Sv over an area of  $(0.2^\circ \text{C} \times 0.04)$  in  $\theta$ -S space. The isopycnal ( $\sigma_2$ )  
 1018 surfaces of  $35.65$  and  $36.58 \text{ kg m}^{-3}$  denote the upper and lower AAIW interfaces

1019

1020 Figure 18: a) Probability map of the trajectory occurrence in the South Atlantic ( $1/4^\circ \times 1/4^\circ$  grid) over the  
 1021 30 year for the 12,554 AAIW particles that were released along  $58^\circ\text{W}$  in the Drake Passage (black line)  
 1022 and reached  $6^\circ\text{S}$  at the end of integration. The four color lines represent the climatological mean location  
 1023 of the ACC fronts from Orsi et al. (1995): the subantarctic front (SAF, red), polar front (PF, green), southern  
 1024 ACC front (SACCF, blue), and southern boundary of the ACC (SBdy, pink). b) averaged “Lagrangian”  
 1025 AAIW transport from the Drake Passage across seven latitudes as a function of integration time.  
 1026

1027 Figure 19. Modeled long-term mean horizontal transport streamfunction for the layer of NADW  
 1028 ( $36.58 < \sigma_2 < 37.12 \text{ kg m}^{-3}$ ). Pink streamlines (10 Sv increment) indicate the eastward transport of the ACC,  
 1029 blue to yellow streamlines (2 Sv increment) represent the southward spreading of the NADW from north.  
 1030

1031 Figure 20. a) Observed and modeled salinity distribution at 2500m in the South Atlantic. Observations are  
 1032 based on CTD data from GoShip program <http://www.go-ship.org>. Detailed vertical sections can be seen  
 1033 in the WOCE Atlas (Kiltermann et al., 2011). The results show an eastward extension of high salinity  
 1034 (NADW signature) between  $20$  and  $25^\circ\text{S}$  west of the mid-Atlantic Ridge (MAR), and significantly lower  
 1035 salinity east of MAR.  
 1036

1037 Figure 21. Zoomed view of the modeled mean circulation for the density layer of NADW ( $36.58 < \sigma_2 < 37.12$   
 1038  $\text{kg m}^{-3}$ ) across the Mid-Atlantic Ridge in the South Atlantic Ocean.  
 1039

1040 Figure 22. Power spectral density of the AMOC variability across different latitude bands, showing a lack  
 1041 of distinct period of the variability across all latitudes except on annual timescale.  
 1042

1043 Figure 23. Modeled seasonal variability of the AMOC transport (in Sv) in the Atlantic basin ( $35^\circ\text{S}$ - $70^\circ\text{N}$ ),  
 1044 based on the 3<sup>rd</sup> Intrinsic mode function (IMF) using the ensemble empirical mode decomposition (EEMD,  
 1045 Wu and Huang 2009). The right panel shows the monthly variability averaged over 1958-2018.  
 1046

1047 Figure 24. Modeled interannual variability of the AMOC transport (in Sv) in the Atlantic basin ( $35^\circ\text{S}$ -  
 1048  $70^\circ\text{N}$ ), based on the 4<sup>th</sup> and 5<sup>th</sup> Intrinsic mode function (IMF).  
 1049

1050 Figure 25. Correlation coefficient between the variability of the domain averaged AMOC transport and the  
 1051 variability of the AMOC transport at each latitude; Red and green are interannual variability (4<sup>th</sup> and 5<sup>th</sup>  
 1052 IMF) shown in Figure 24 and blue is decadal variability (6<sup>th</sup> IMF) shown in Figure 26.  
 1053

1054 Figure 26. Modeled decadal and longer-term variability of the AMOC transport (in Sv) in the Atlantic Basin  
 1055 ( $35^\circ\text{S}$ - $70^\circ\text{N}$ ), based on the 6<sup>th</sup> and the sum of 7<sup>th</sup> to 9<sup>th</sup> Intrinsic mode function (IMF), respectively.  
 1056

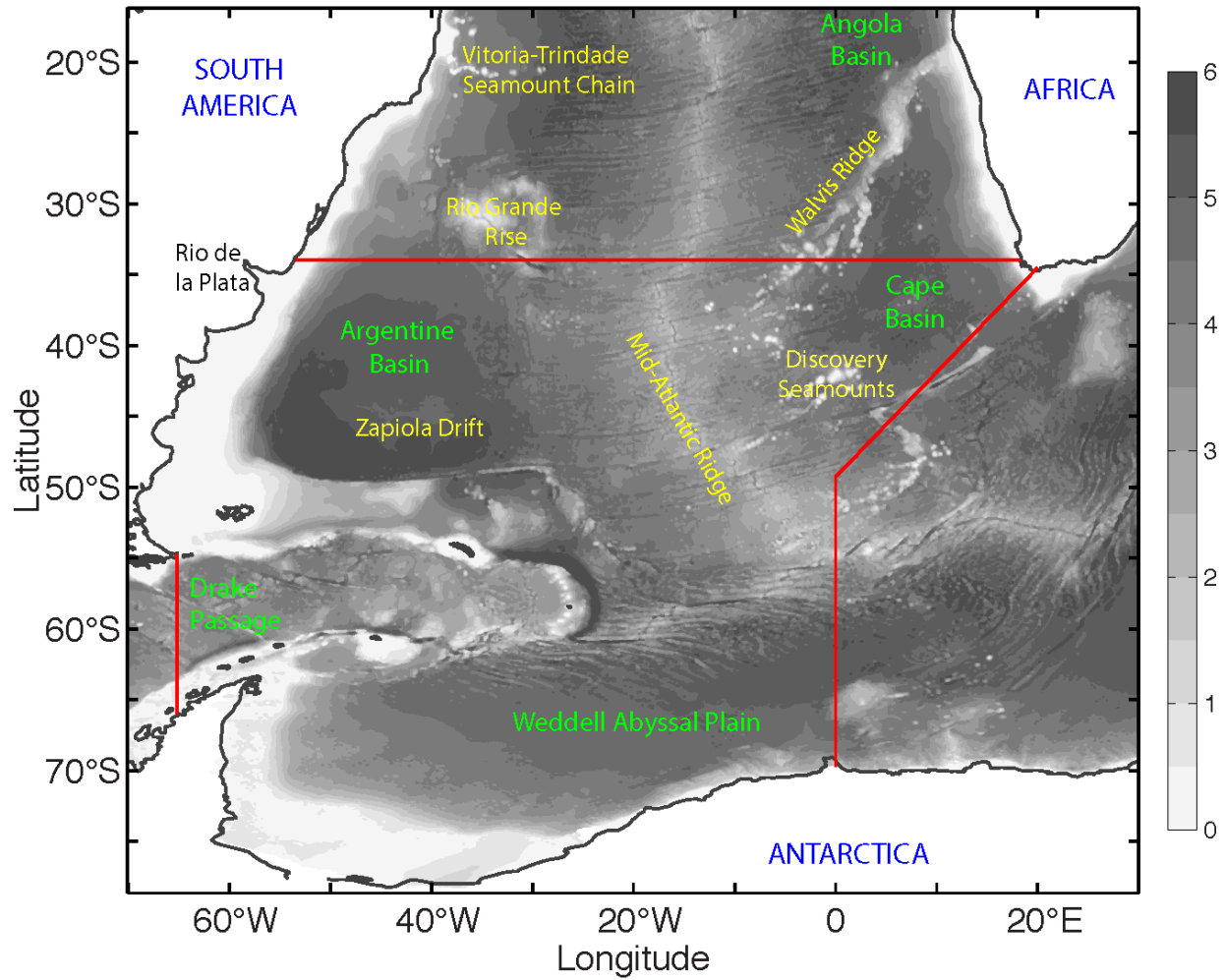


Figure 1: Model bathymetry (in km) along with key topographic features in the South Atlantic Ocean. Red lines denote three sections where significant observations have been obtained and the observations are used to evaluate the model results: 34°S in the South Atlantic, 65°W in Drake Passage, and the Prime Meridian-Good Hope (PM-GH) transect southwest of Africa.

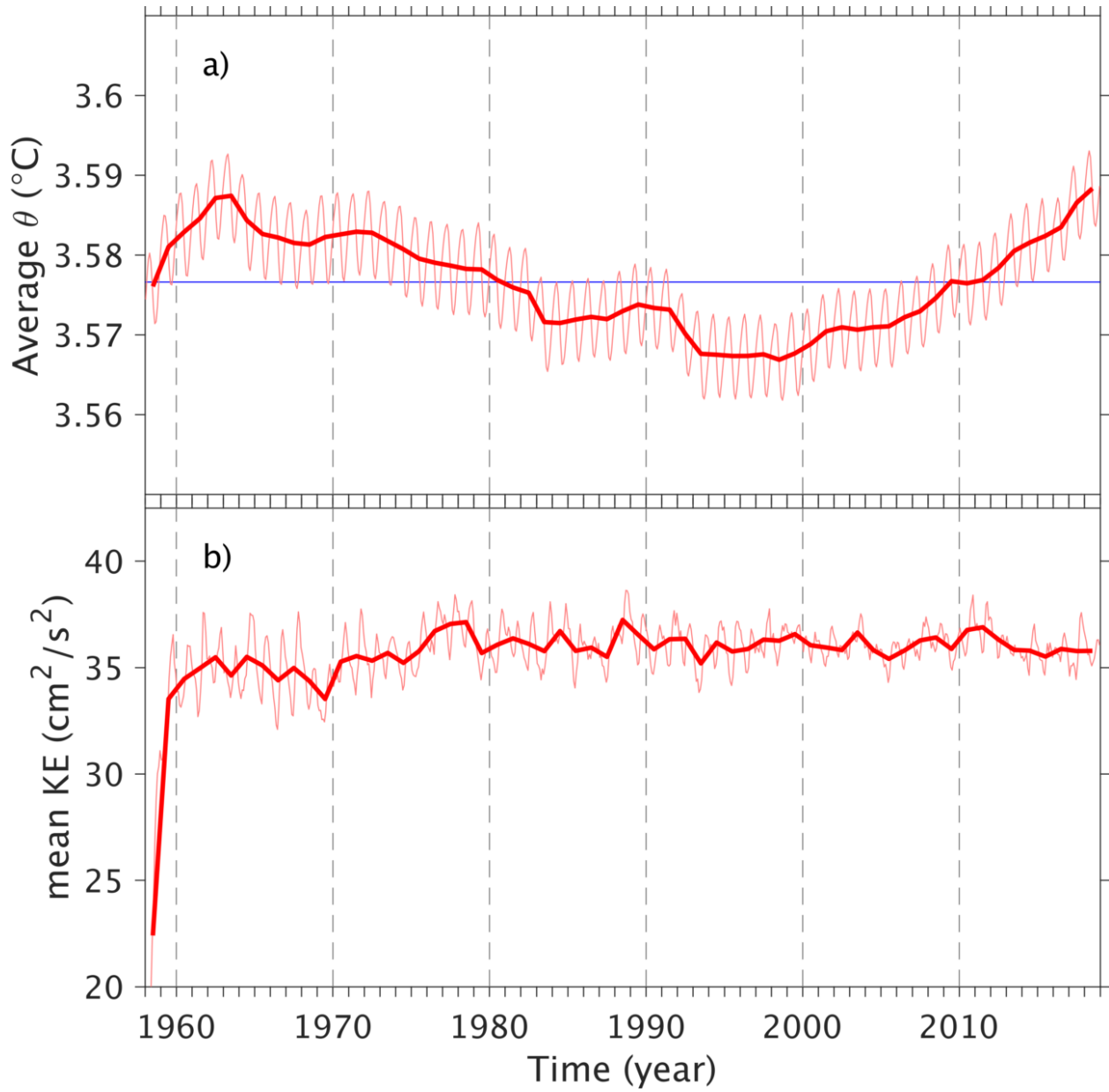


Figure 2: Time evolution of global domain-averaged a) potential temperature in  $^{\circ}\text{C}$  and b) total kinetic energy in  $\text{cm}^2/\text{s}^2$  from the global ocean-sea ice simulation. Thin and thick lines denote monthly and annual means, respectively.

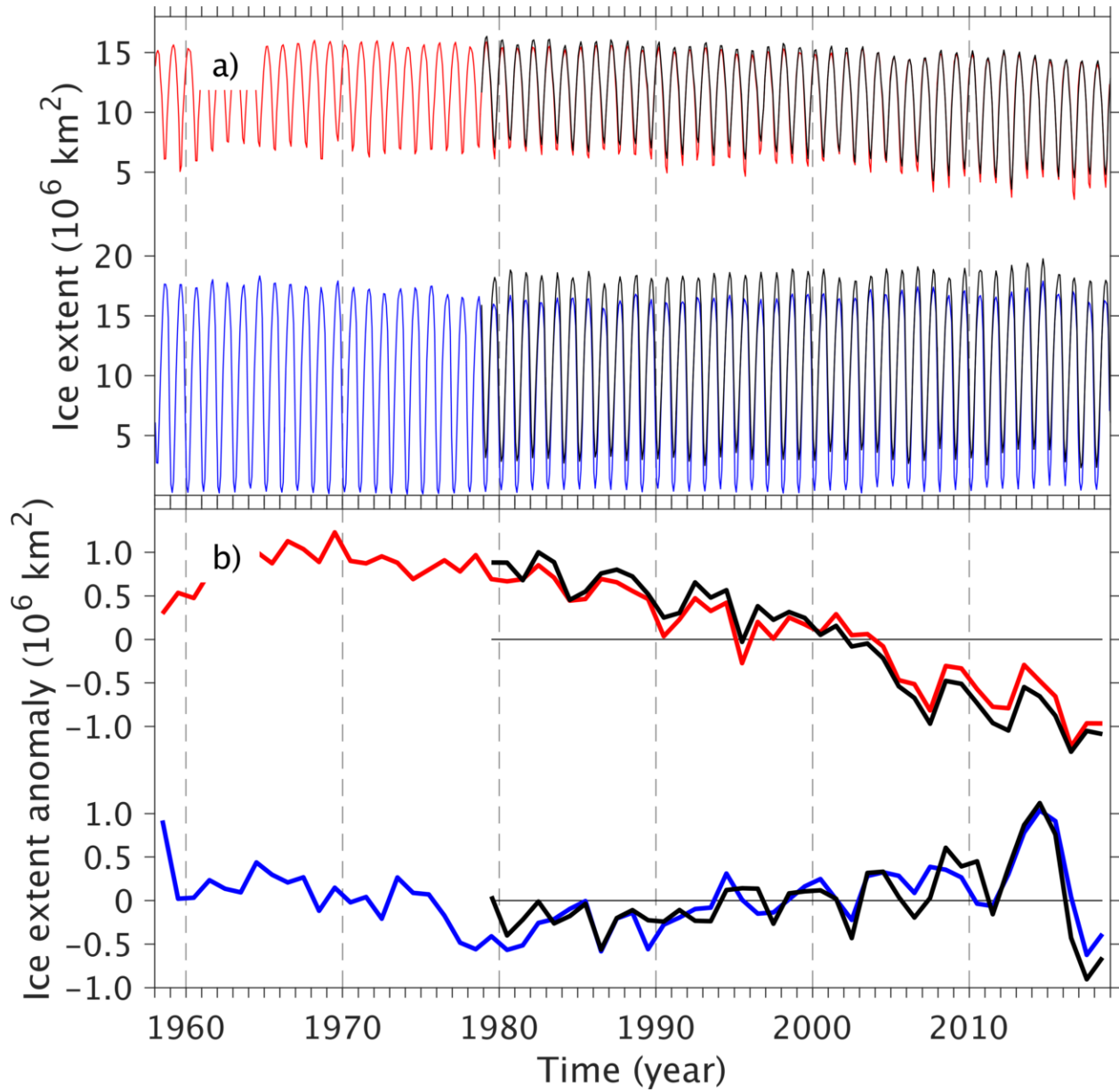


Figure 3: Time evolution of a) monthly mean sea ice extent and b) annual mean sea ice extent anomaly relative to the 1980-2015 average. The sea ice extent is defined as the area (in  $10^6 \text{ km}^2$ ) with sea ice concentration of 15% or higher. The red/blue lines are model results in the northern/ southern hemisphere; black lines are observations from National Snow and Ice Data Center.

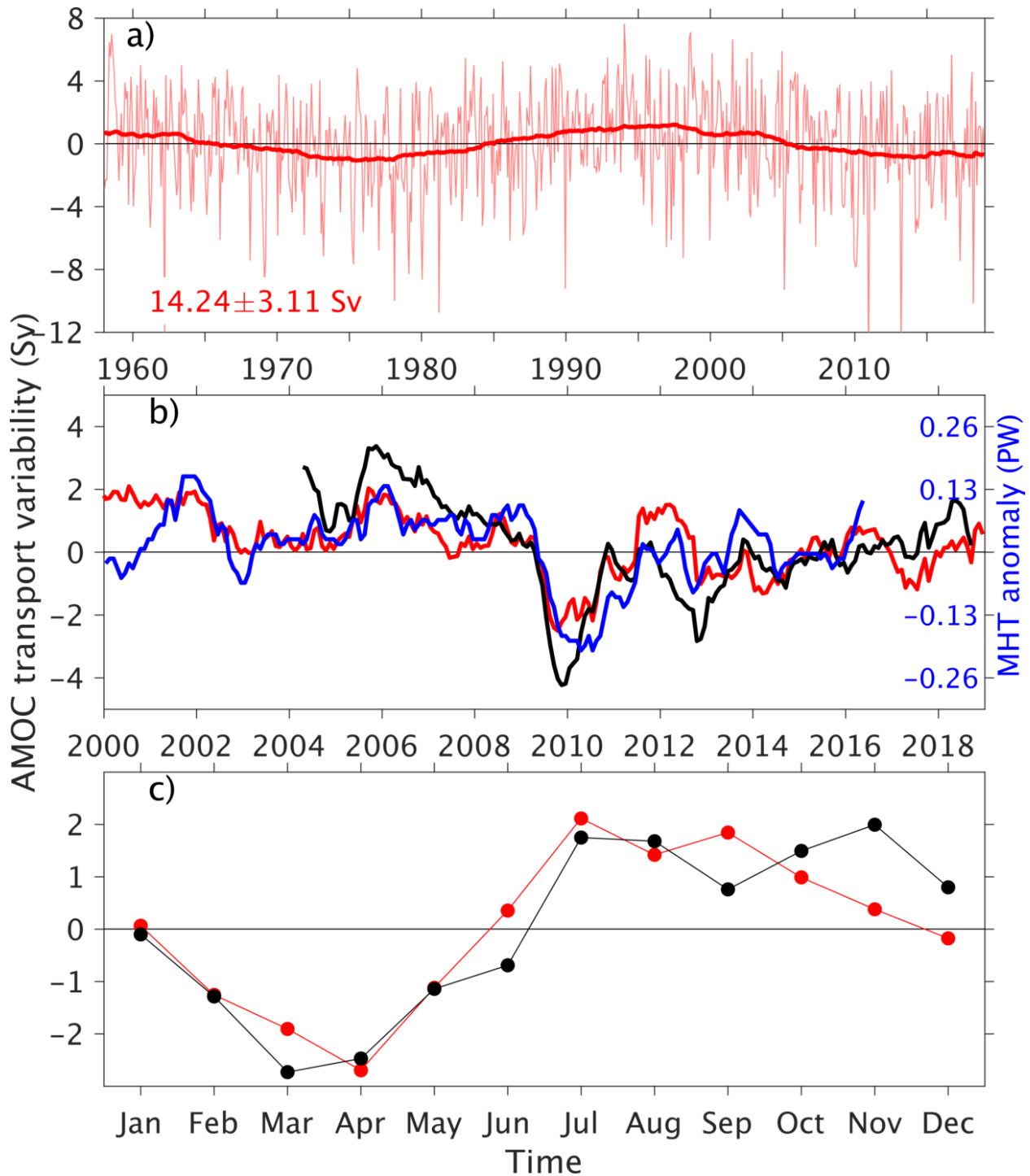


Figure 4. a) Time evolution of the modeled monthly mean transport of the Atlantic meridional overturning circulation (AMOC) at 26.5°N; thick line denotes a 10-year averages; b) Variability of the modeled AMOC transports (red line), the observed AMOC transports (black line) from the RAPID array (e.g., Smeed et al., 2018), and the observed meridional heat transport (MHT, blue line) from Trenberth et al. (2019), all in 12-month moving average; c) Seasonal variability of the AMOC transports at 26.56°N averaged over 2004-2017 from model (red line) and the RAPID array (black line).

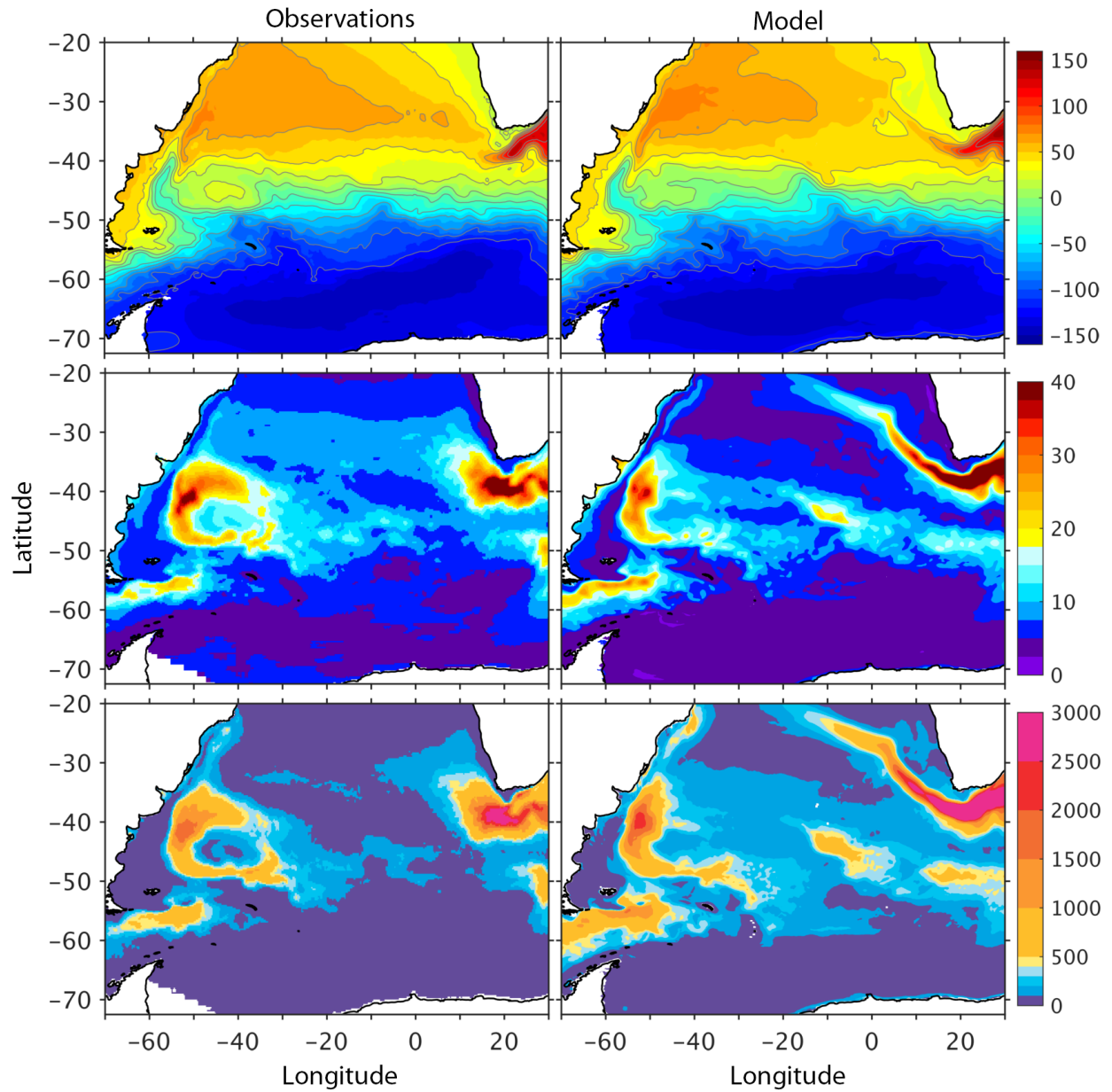


Figure 5. Observed and modeled distributions of a-b) time mean sea surface height (SSH, in cm), c-d) SSH standard deviation (in cm), and e-f) eddy kinetic energy (EKE, in  $\text{cm}^2 \text{s}^{-2}$ ) of the surface current in the southern Atlantic. In observation, the mean SSH is based on long-term climatology CNES-CLS18 (Rio et al., 2019); the SSH standard deviation and EKE are based on AVISO data in 1993-2018. All model results are also in 1993-2018.

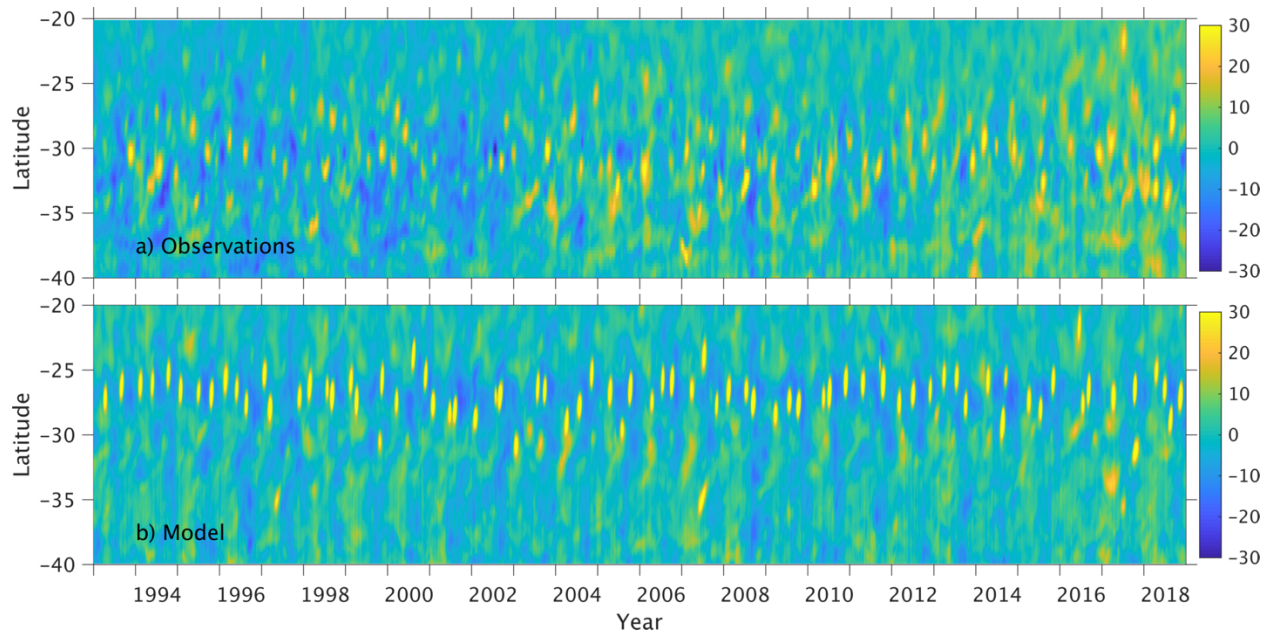


Figure 6: Observed and modeled sea-surface height (SSH) anomaly along the Prime Meridian in latitude range 20-40°S from 1993 to 2018. The high SSH anomaly denotes the west-/northwestward translation of the Agulhas Rings that pass the Prime Meridian.

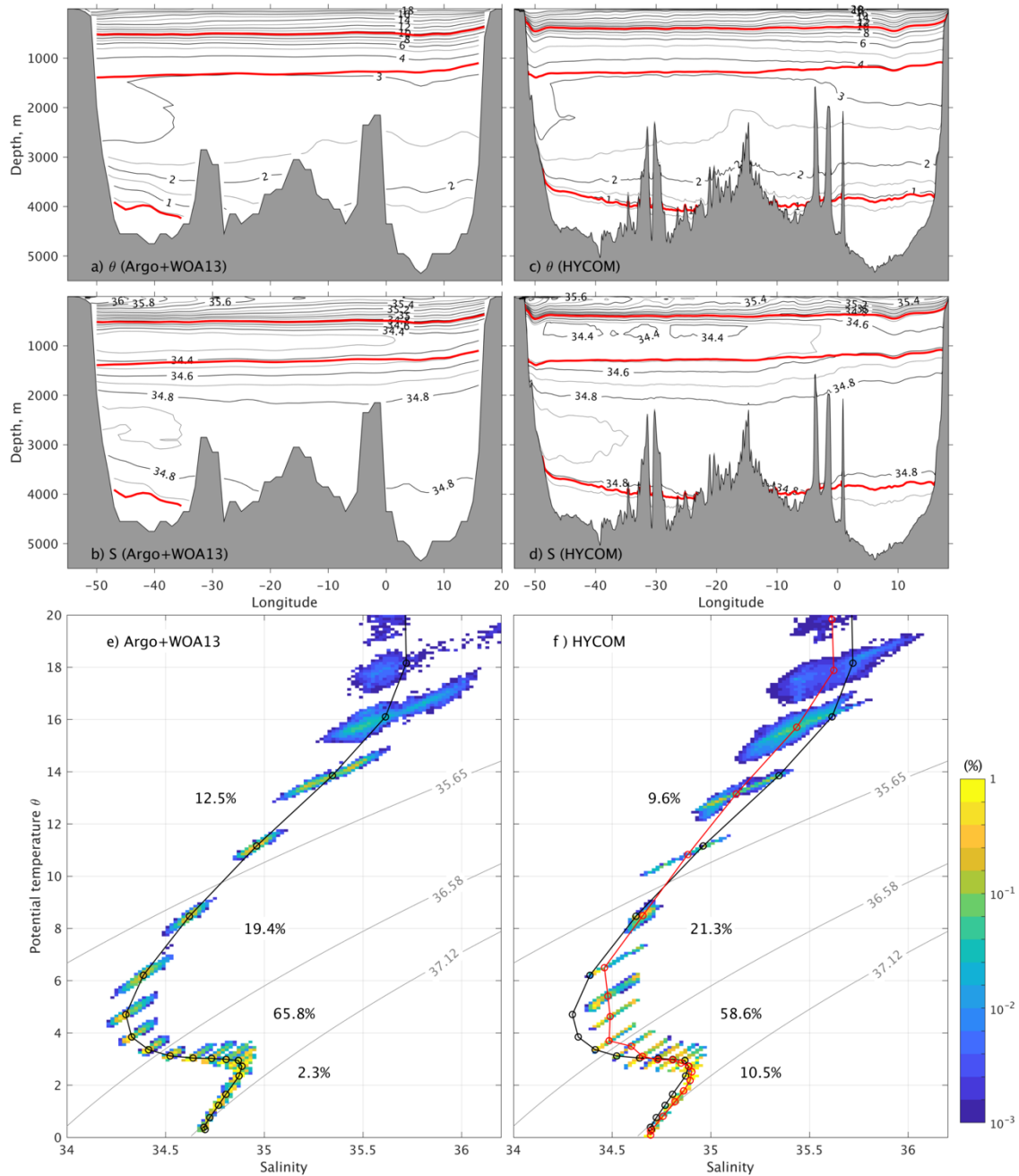


Figure 7. a-d) Potential temperature  $\theta$  and salinity  $S$  distributions across 34°S. Observations are based on a combination of Argo profiles for the top 2000 m and World Ocean Atlas 2013 (WOA13) below 2000 m; model results are from the global 1/12° HYCOM simulation. Three red lines denote isopycnic surfaces ( $\sigma_2$  of 35.65, 36.58, and 37.12  $\text{kg m}^{-3}$ ) that divide the water column into near surface water, Antarctic Intermediate Water (AAIW), North Atlantic Deep Water (NADW), and Antarctic Bottom Water (AABW). e-f) Volumetric  $\theta$ - $S$  diagram along 34°S. Color shading shows the volume percentage for water mass with  $\Delta\theta$ ,  $\Delta S$  resolution of 0.1°C, 0.02 psu (percentages for near surface water, AAIW, NADW and AABW are also listed); circled lines are volume-weighted  $\theta$ - $S$  profile in observations (black) and model results (red).

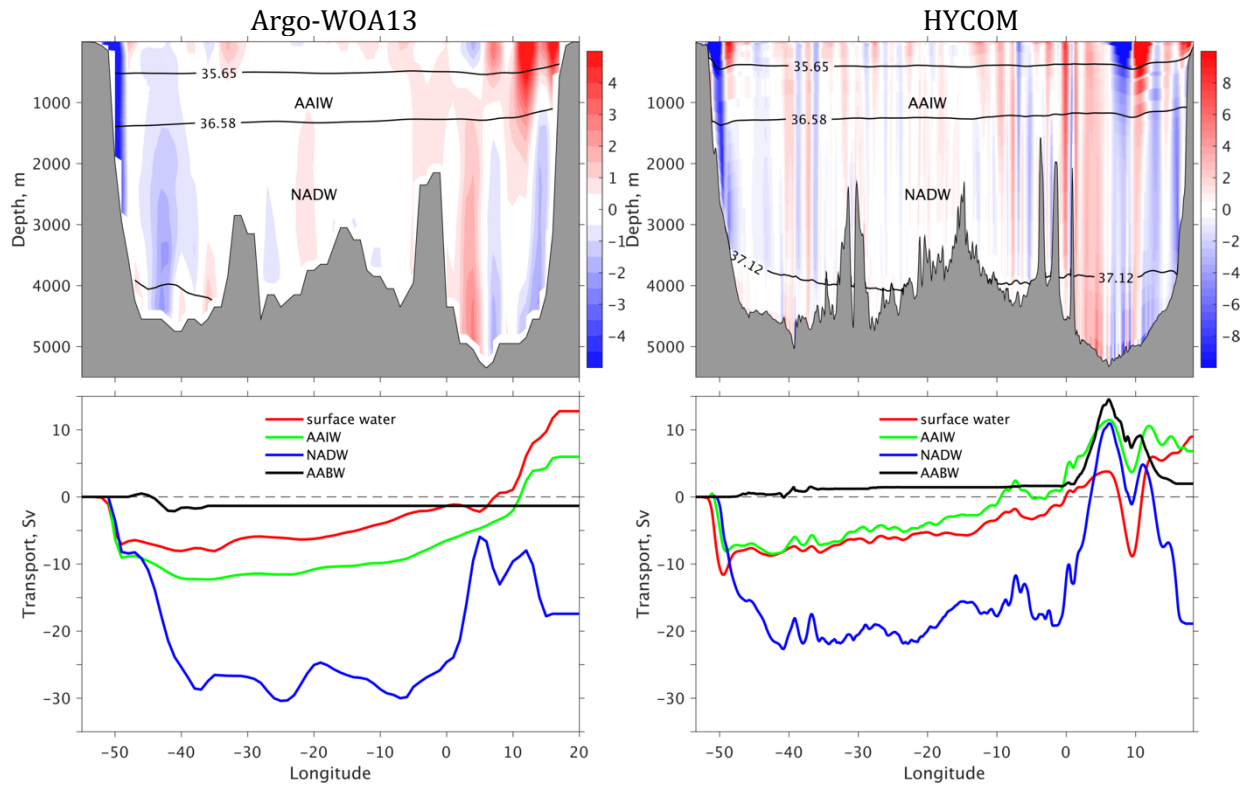


Figure 8. Observed and modeled time mean meridional velocity across 34°S and the corresponding volume transport for the four density layers: near surface water ( $\sigma_2 < 35.65 \text{ kg m}^{-3}$ ), Antarctic Intermediate Water (AAIW,  $35.65 < \sigma_2 < 36.58$ ), North Atlantic Deep Water (NADW,  $36.58 < \sigma_2 < 37.12$ ), and Antarctic Bottom Water (AABW,  $\sigma_2 > 37.12$ ). Observations are based on a combination of Argo-WOA13 profiles; model results based on the global 1/12° HYCOM simulation.

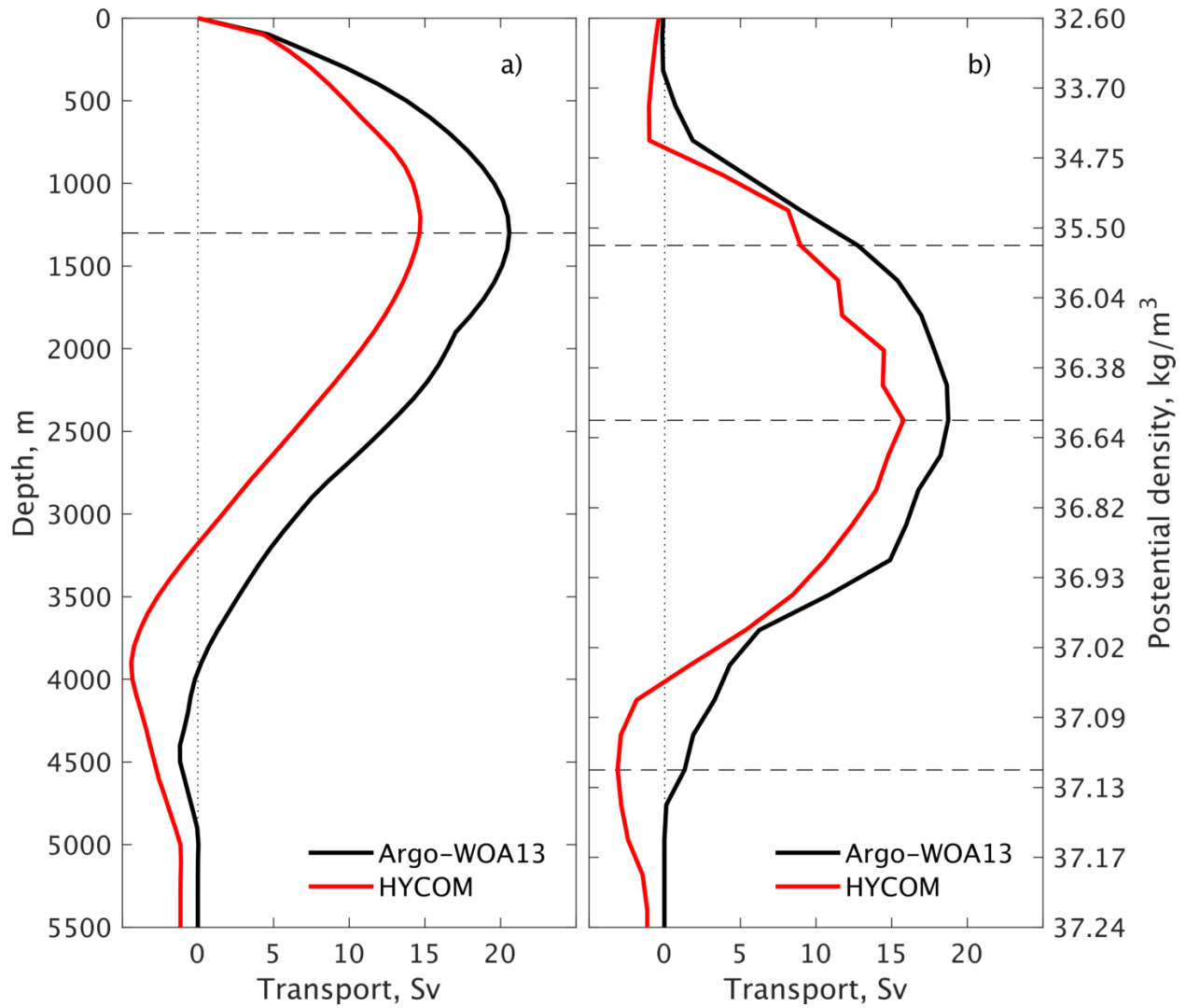


Figure 9. Long-term mean meridional overturning streamfunction (in Sv) at 34°S with respect to a) depth and b) potential density in  $\sigma_2$ . Observations based on monthly mean Argo-WOA13 profiles; model results based a global 1/12° HYCOM simulation (1979-2018).

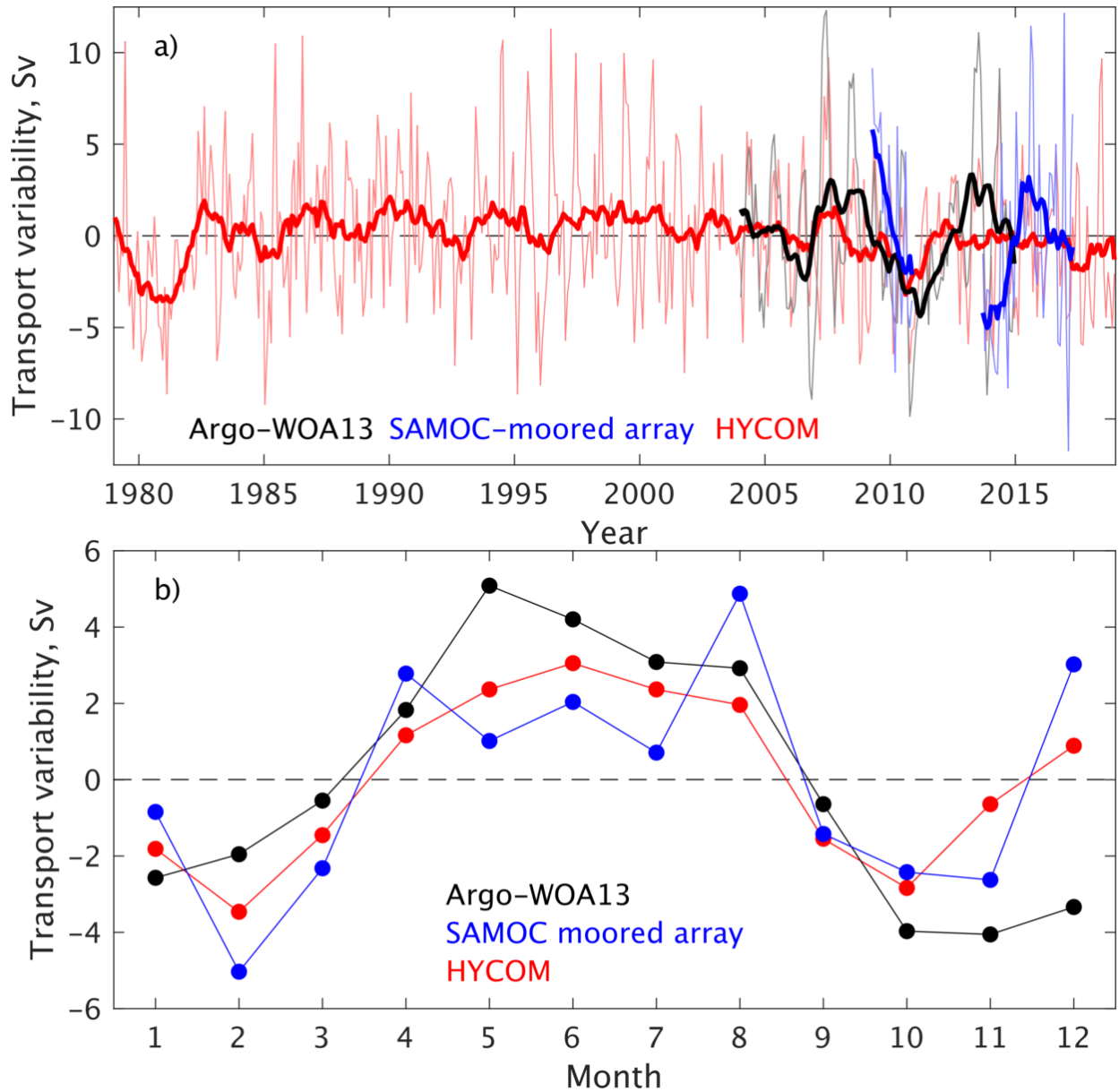


Figure 10: a) Time series of the AMOC transport variability (in Sv) at 34°S based on Argo-WOA13 (black, Dong et al., 2014), SAMOC-mooring array (blue, Meinen et al., 2018), and global HYCOM (red). The thin and thick lines represent monthly means and 12-month moving averages, respectively. b) AMOC transport variability at seasonal timescale, with each dot representing the multi-year average of the monthly AMOC transport.

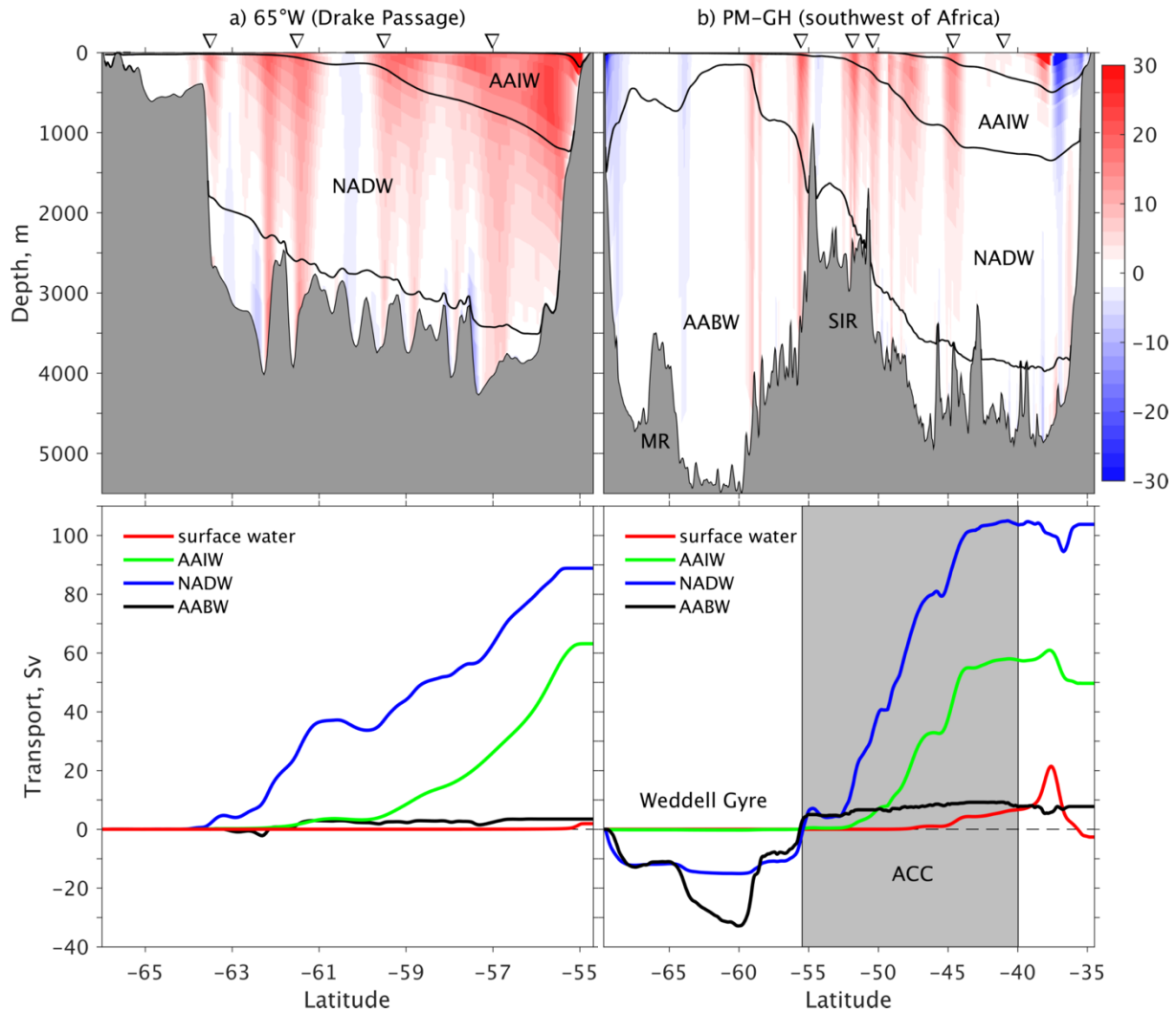


Figure 11: Modeled long-term mean zonal velocity and the corresponding four-layer volume transport in four density layers across a)  $65^{\circ}\text{W}$  in the Drake Passage and b) the Prime Meridian-Good Hope (PM-GH) transect southwest of Africa. The triangles denote the locations of Antarctic circumpolar current (ACC) fronts, from south to north, the Southern Boundary, South ACC Front, Polar Front, Subantarctic Front, and the subtropical front in panel b. The shaded area in panel b) between  $40$  and  $55.5^{\circ}\text{S}$  marks the ACC regime across the PM-GH transect. Transport is accumulative northward. The four layers are near surface water ( $\sigma_2 < 35.65 \text{ kg m}^{-3}$ ), Antarctic Intermediate Water (AAIW,  $35.65 < \sigma_2 < 36.58$ ), North Atlantic Deep Water (NADW,  $36.58 < \sigma_2 < 37.12$ ), and Antarctic Bottom Water (AABW,  $\sigma_2 > 37.12$ ).

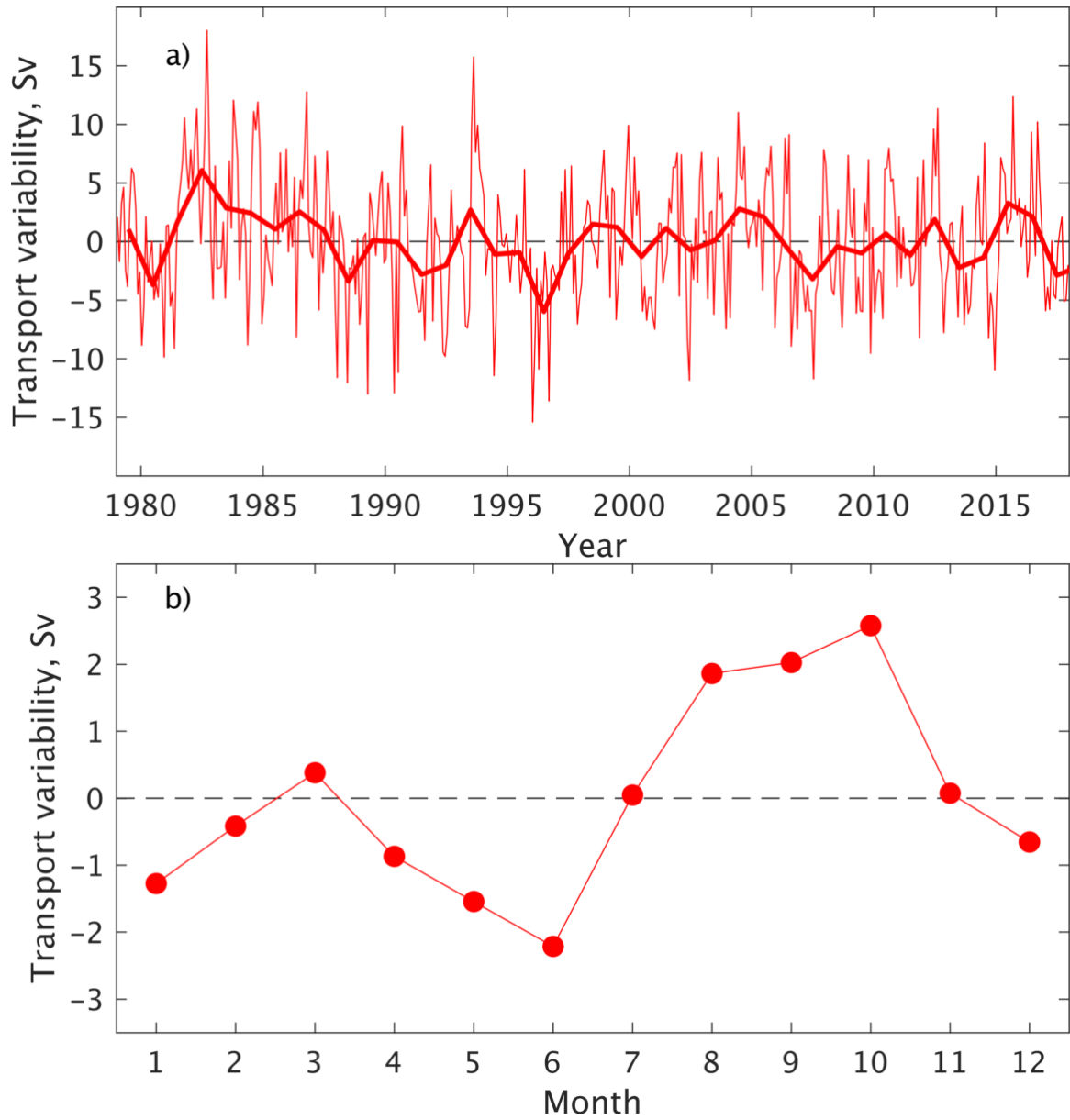


Figure 12: a) Variability of the modeled ACC transport through the Drake Passage at the 65°W, with thin and thick lines represent monthly means and annual means, respectively; b) Seasonal variability of the modeled ACC transports averaged over 1979-2018.

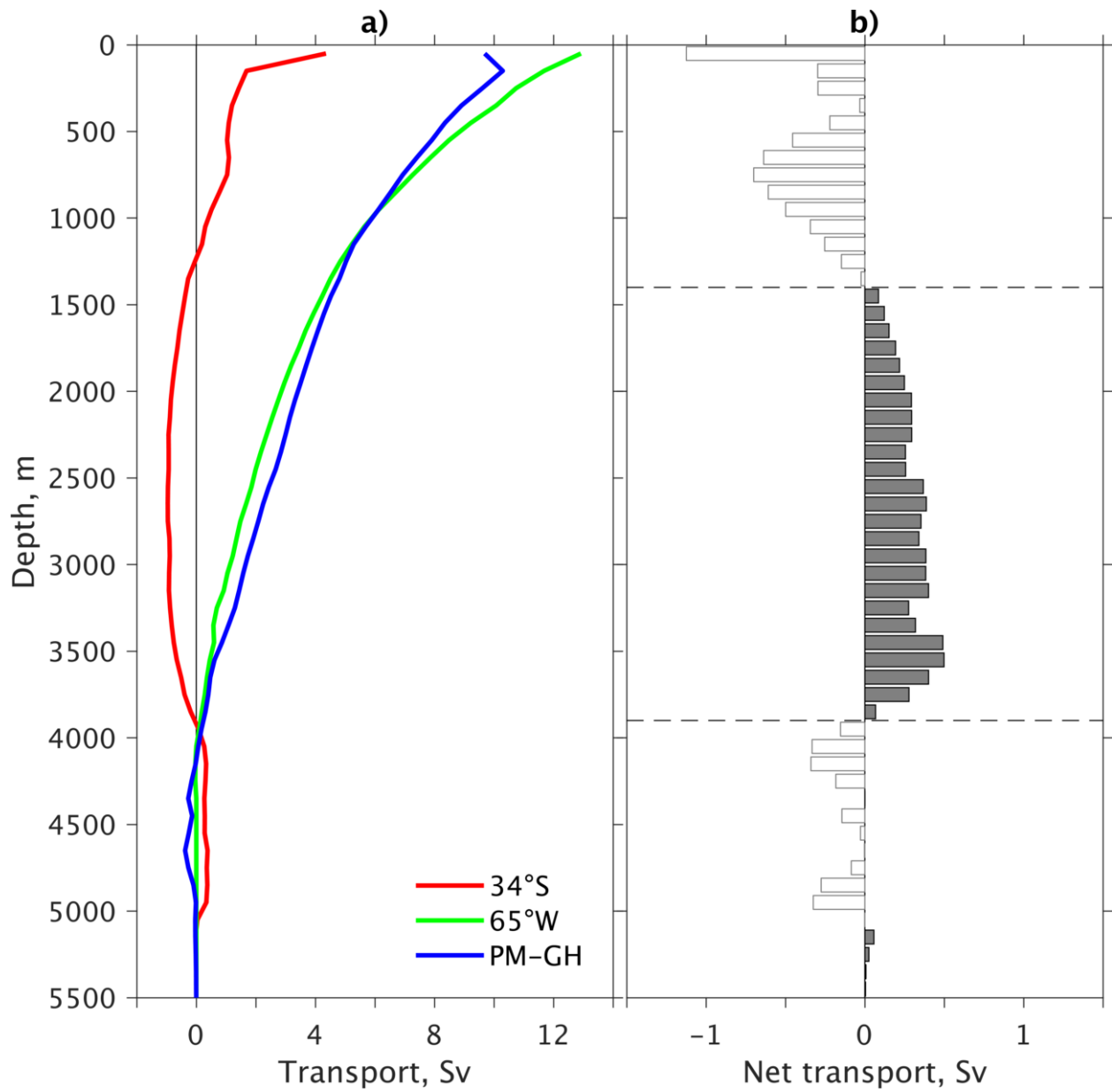


Figure 13: a) Modeled mean horizontal transports (Sv per 100m) in the vertical across the 34°S, the 65°W, and the PM-GH transects; b) The net transports into the region enclosed by the three transects, with positive (negative) values indicating net transport into (out of) the region.

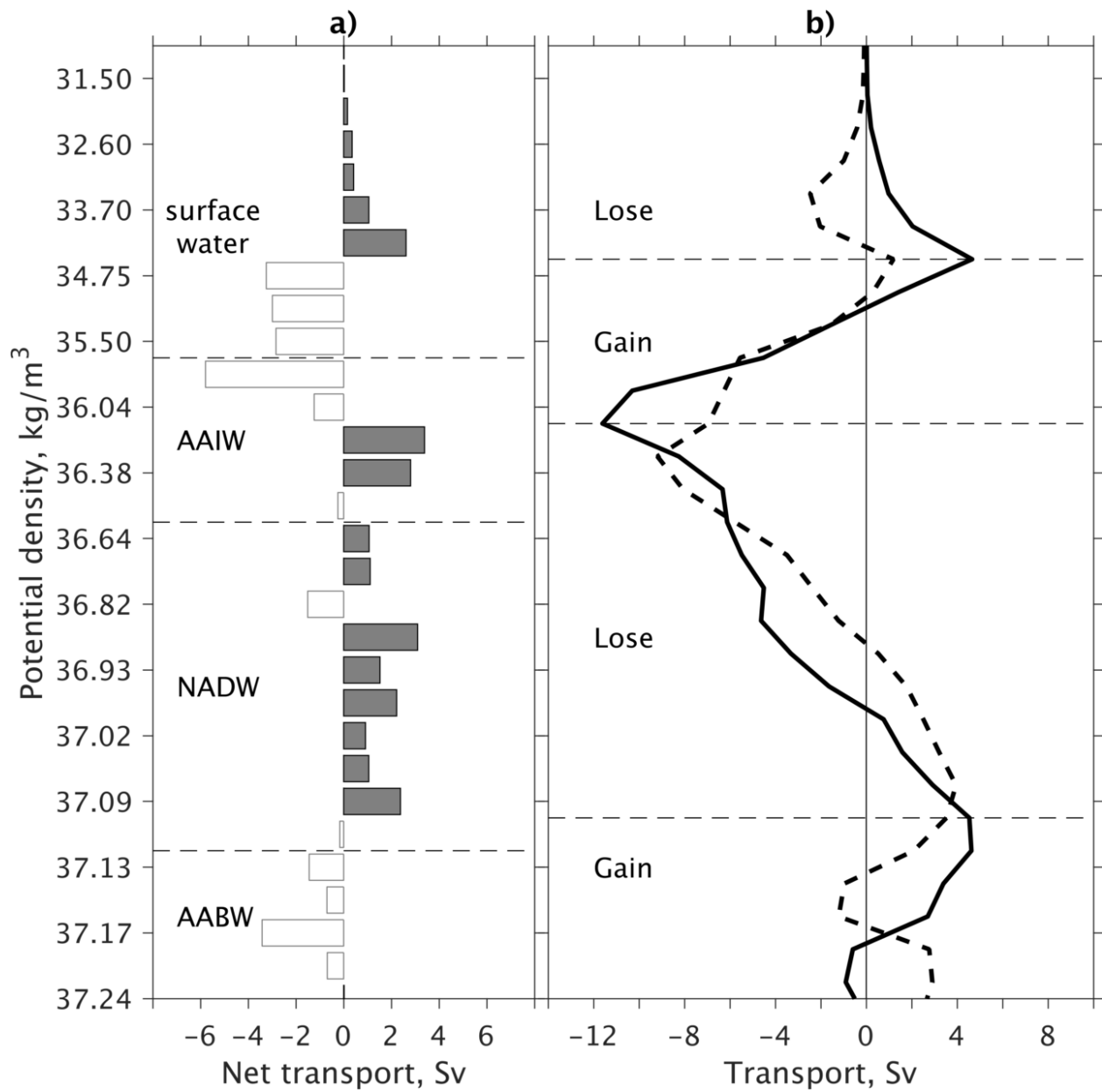


Figure 14: a) Net transports into the South Atlantic region enclosed by the 34°S, the 65°W, and the PM-GH transects, with respect to density layers (positive/negative values for net transport into/out of the region); b) Solid line denotes the total diapycnal transformation; dashed line denotes the diapycnal transformation calculated from surface buoyancy fluxes.

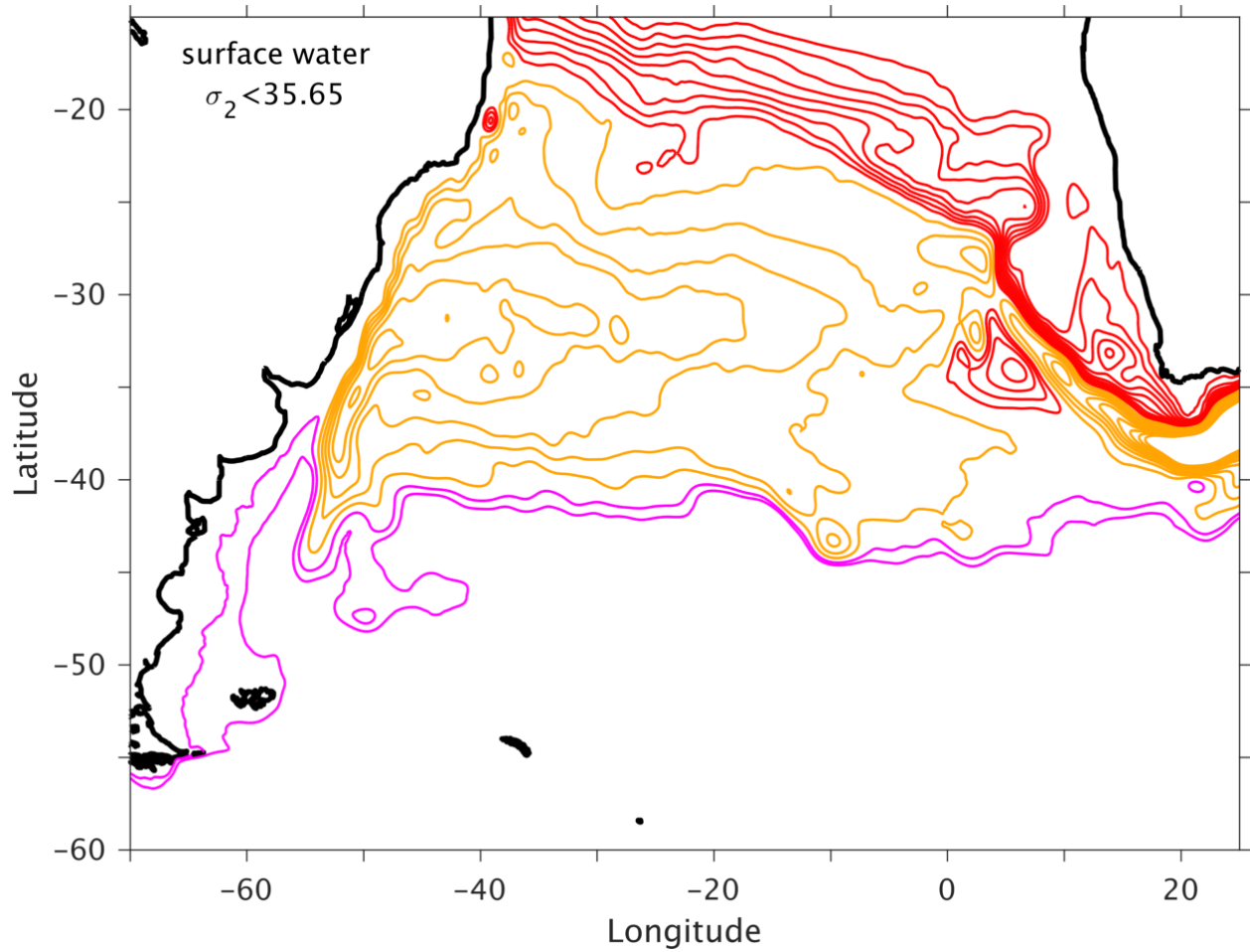


Figure 15: Modeled long-term mean horizontal transport streamfunction (in Sv) for the layer of near surface water ( $\sigma_2 < 35.65 \text{ kg m}^{-3}$ ). Red and pink streamlines (increment of 1 Sv) denote AMOC contribution and ACC flow; orange streamlines (increment of 2 Sv) denote the subtropical gyre of the South Atlantic.

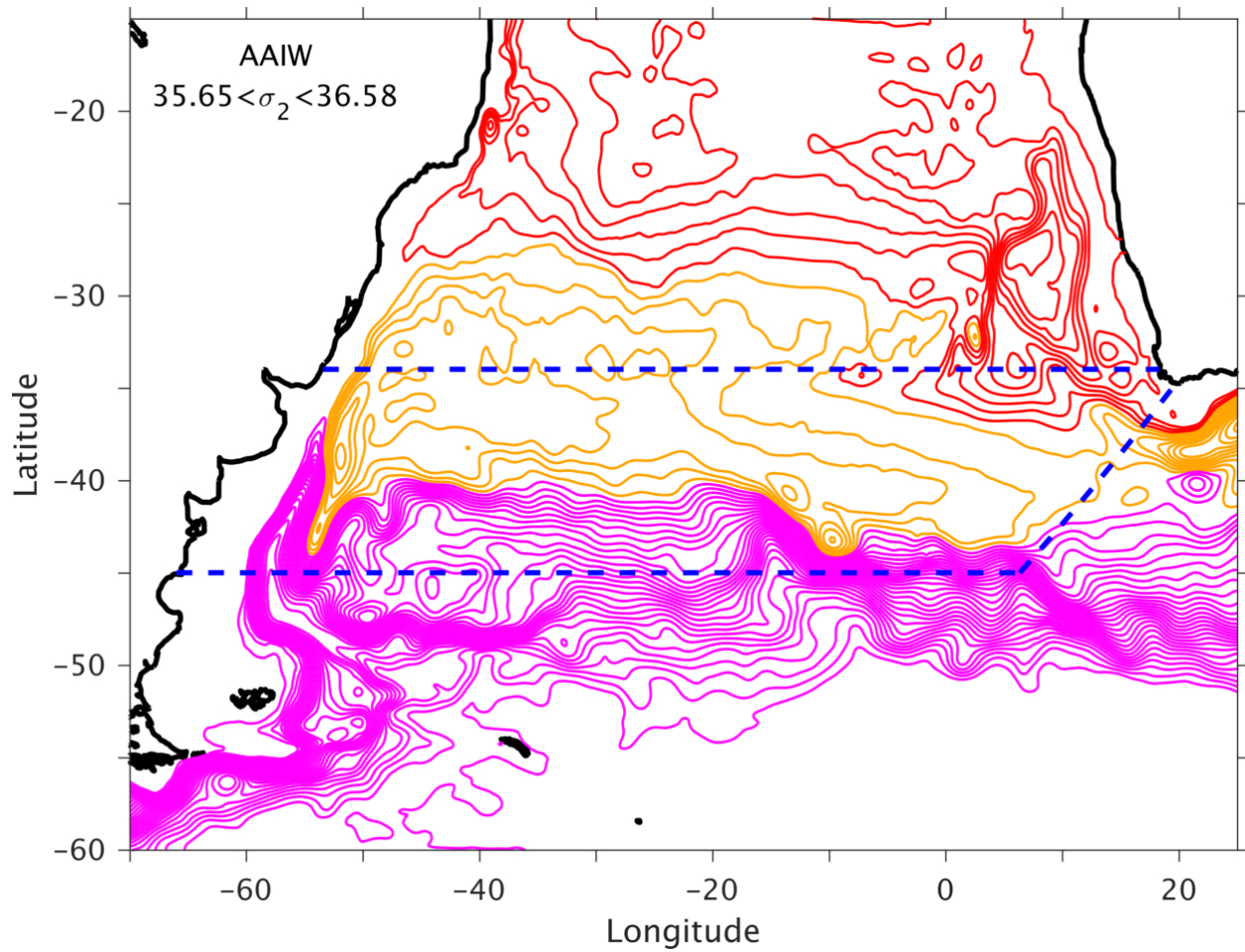


Figure 16: Modeled long-term mean horizontal transport streamfunction (Sv) for the layer of AAIW ( $35.65 < \sigma_2 < 36.58 \text{ kg m}^{-3}$ ). Pink streamlines (increment of 4 Sv) is the ACC; red and orange streamlines denote AMOC contribution and the subtropical gyre of the South Atlantic (similar to Figure 15). The dashed blue lines denote 34°S, 45°S, and the GoodHope sections, across which the water properties of the northward and northwestward transports are examined in Figure 17.

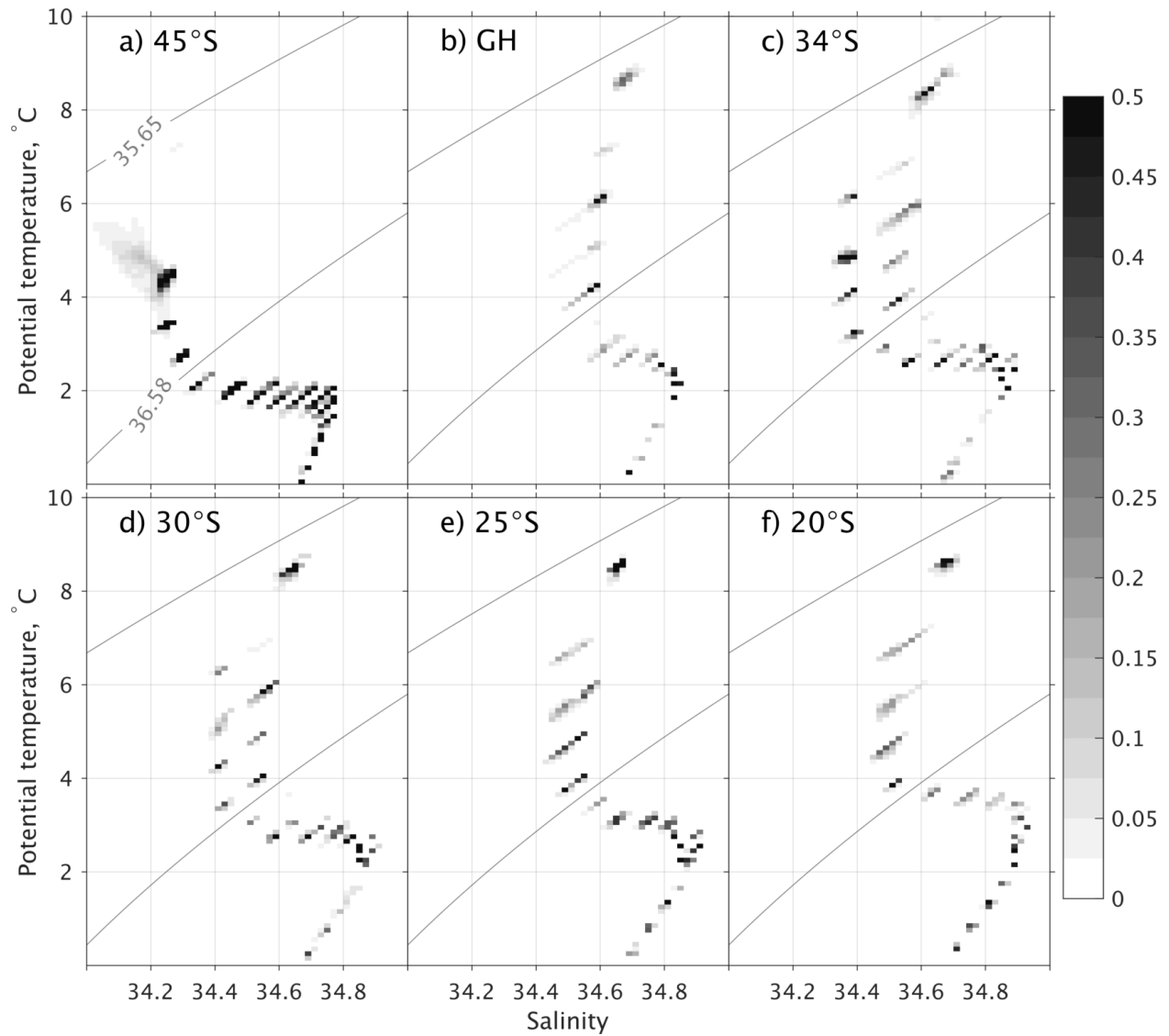


Figure 17: Modeled northward transports projected on potential temperature-salinity ( $\theta$ -S) plane across 6 sections; the transport presented in Sv over an area of  $(0.2^\circ\text{C}\times 0.04)$  in  $\theta$ -S space. The isopycnal ( $\sigma_2$ ) surfaces of  $35.65$  and  $36.58$   $\text{kg m}^{-3}$  denote the upper and lower AAIW interfaces.

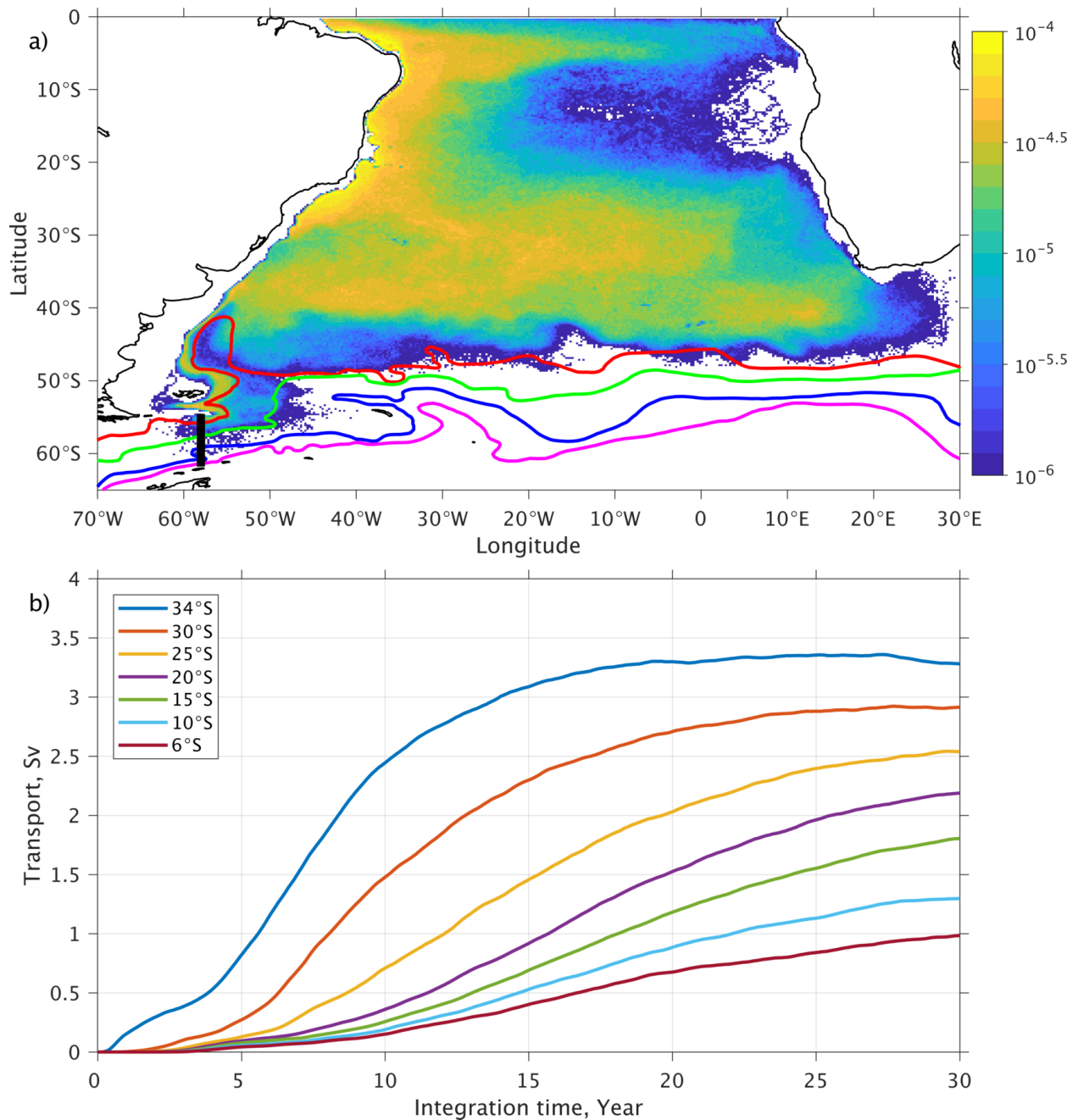


Figure 18: a) Probability map of the trajectory occurrence in the South Atlantic ( $1/4^\circ \times 1/4^\circ$  grid) over the 30 year for the 12,554 AAIW particles that were released along  $58^\circ\text{W}$  in the Drake Passage (black line) and reached  $6^\circ\text{S}$  at the end of integration. The four color lines represent the climatological mean location of the ACC fronts from Orsi et al. (1995): the subantarctic front (SAF, red), polar front (PF, green), southern ACC front (SACCF, blue), and southern boundary of the ACC (SBdy, pink). b) averaged "Lagrangian" AAIW transport from the Drake Passage across seven latitudes as a function of integration time.

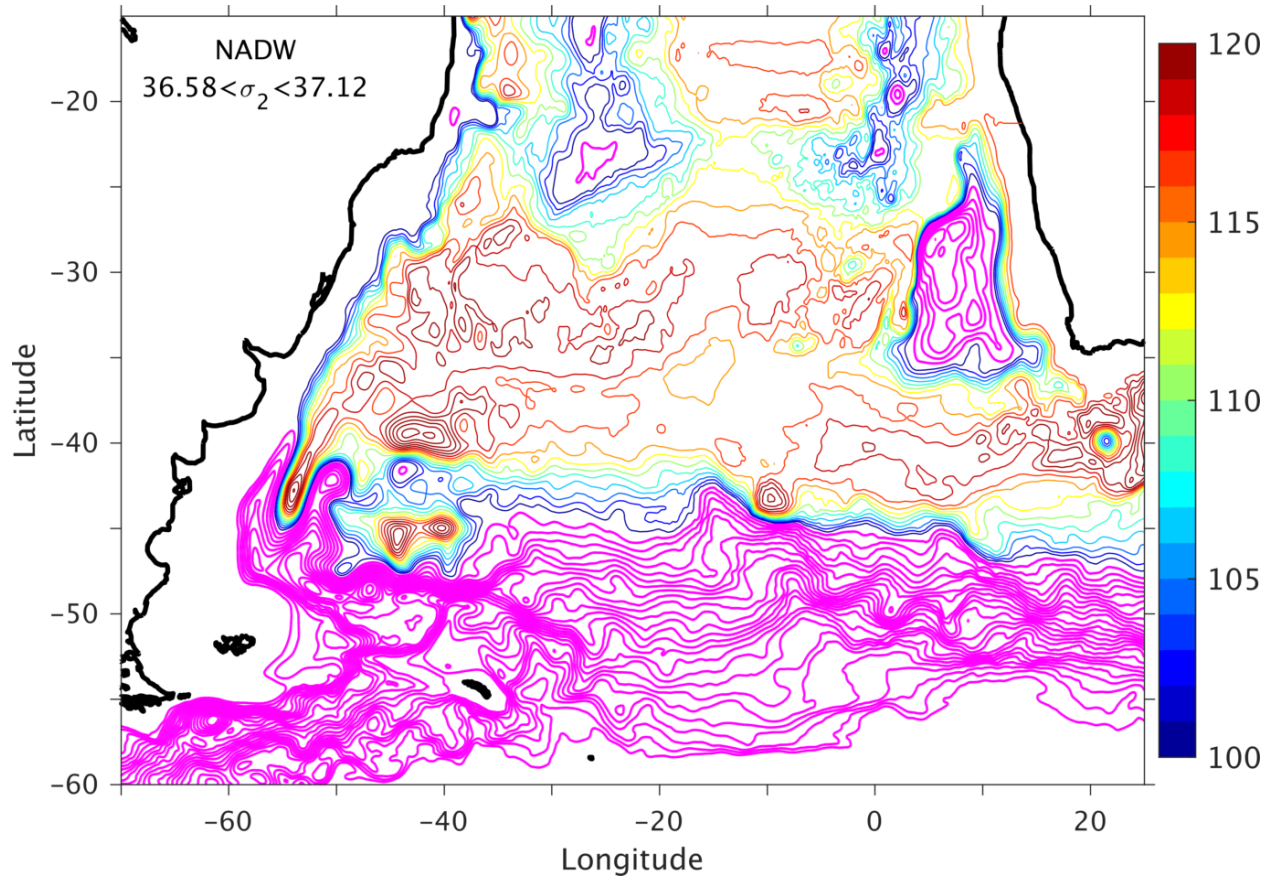


Figure 19. Modeled long-term mean horizontal transport streamfunction for the layer of NADW ( $36.58 < \sigma_2 < 37.12 \text{ kg m}^{-3}$ ). Pink streamlines (10 Sv increment) indicate the eastward transport of the ACC, blue to yellow streamlines (2 Sv increment) represent the southward spreading of the NADW from north.

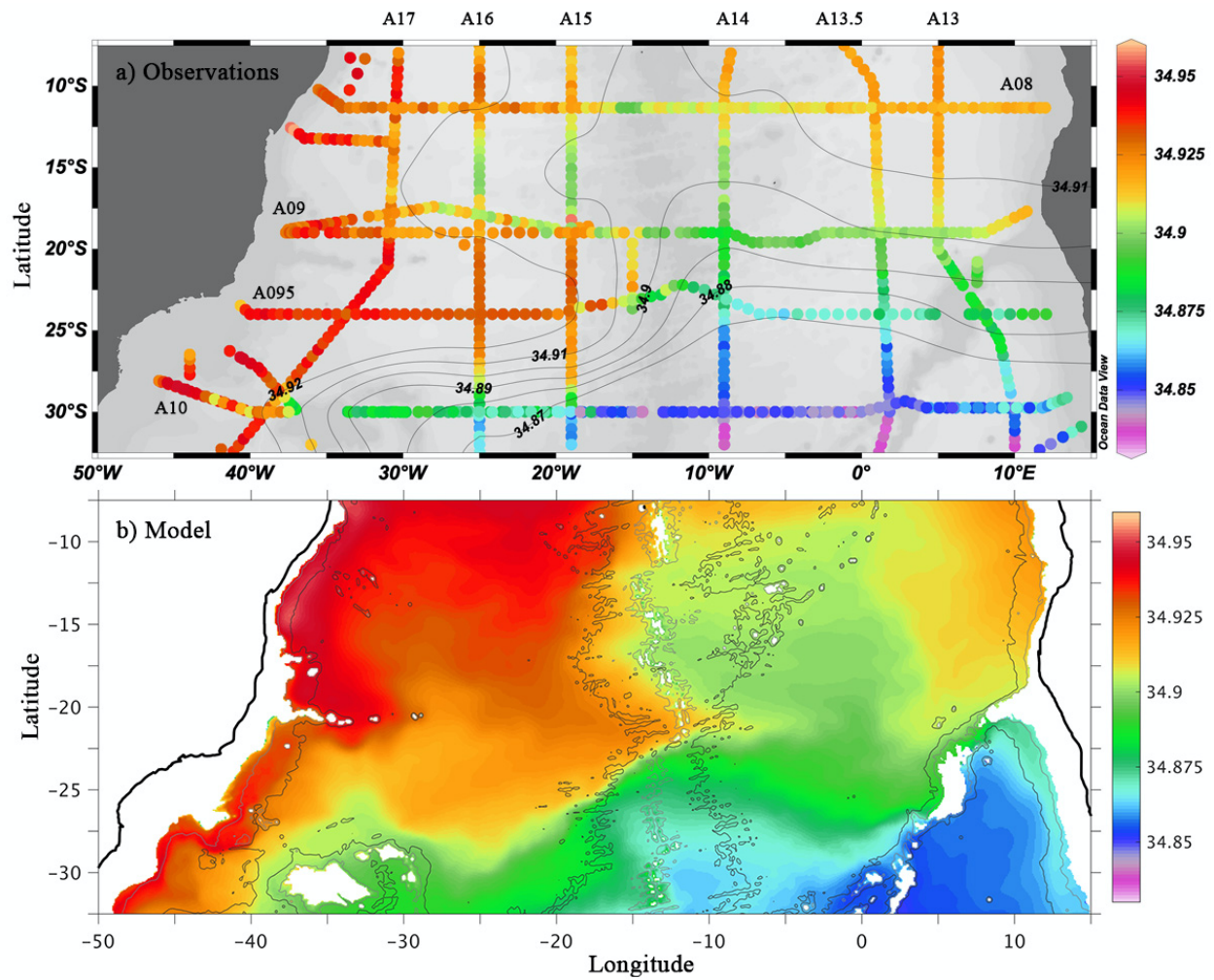


Figure 20. a) Observed and modeled salinity distribution at 2500m in the South Atlantic. Observations are based on CTD data from GoShip program <http://www.go-ship.org>. Detailed vertical sections can be seen in the WOCE Atlas (Kiltermann et al., 2011). The results show an eastward extension of high salinity (NADW signature) between 20 and 25°S west of the mid-Atlantic Ridge (MAR), and significantly lower salinity east of MAR.

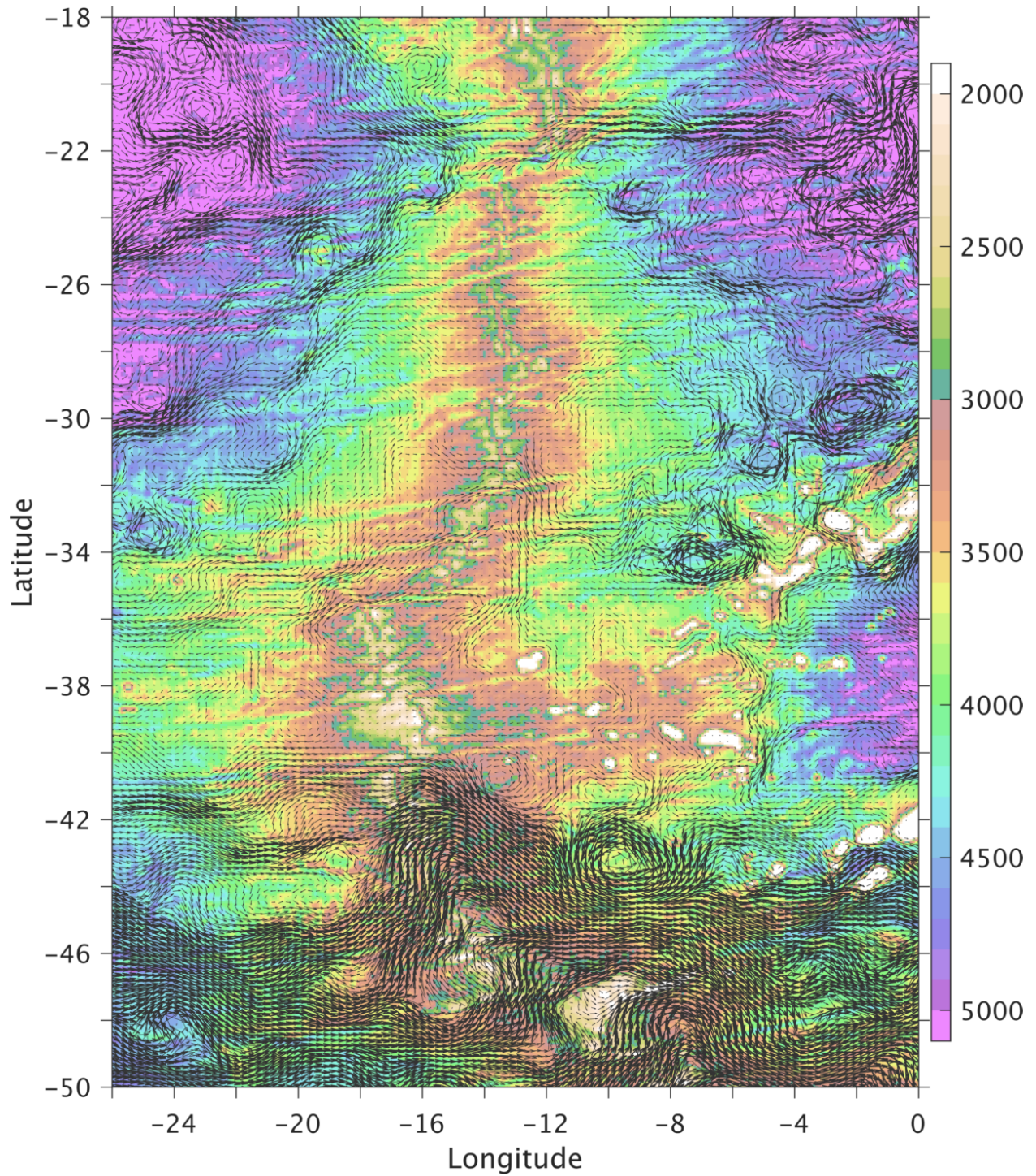


Figure 21. Zoomed view of the modeled mean circulation for the density layer of NADW ( $36.58 < \sigma_2 < 37.12$   $\text{kg m}^{-3}$ ) across the Mid-Atlantic Ridge in the South Atlantic Ocean.

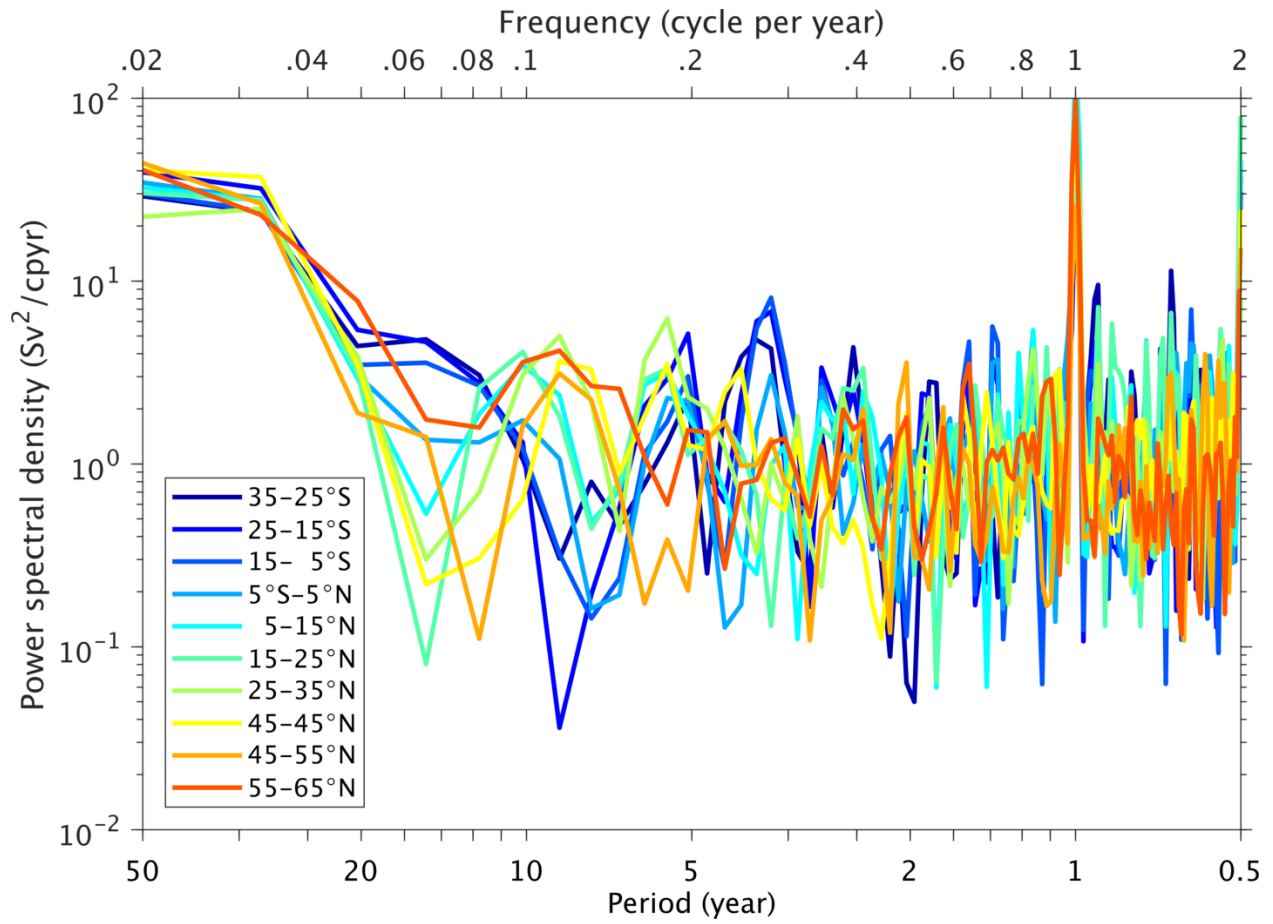


Figure 22. Power spectral density of the AMOC variability across different latitude bands, showing a lack of distinct period of the variability across all latitudes except on annual timescale.

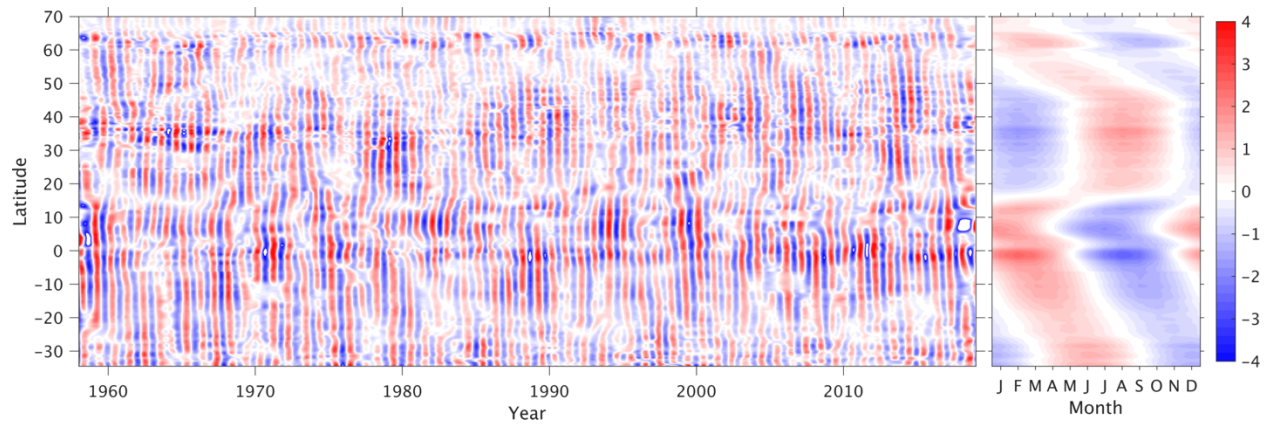


Figure 23. Modeled seasonal variability of the AMOC transport (in Sv) in the Atlantic basin (35°S-70°N), based on the 3<sup>rd</sup> Intrinsic mode function (IMF) using the ensemble empirical mode decomposition (EEMD, Wu and Huang 2009). The right panel shows the monthly variability averaged over 1958-2018.

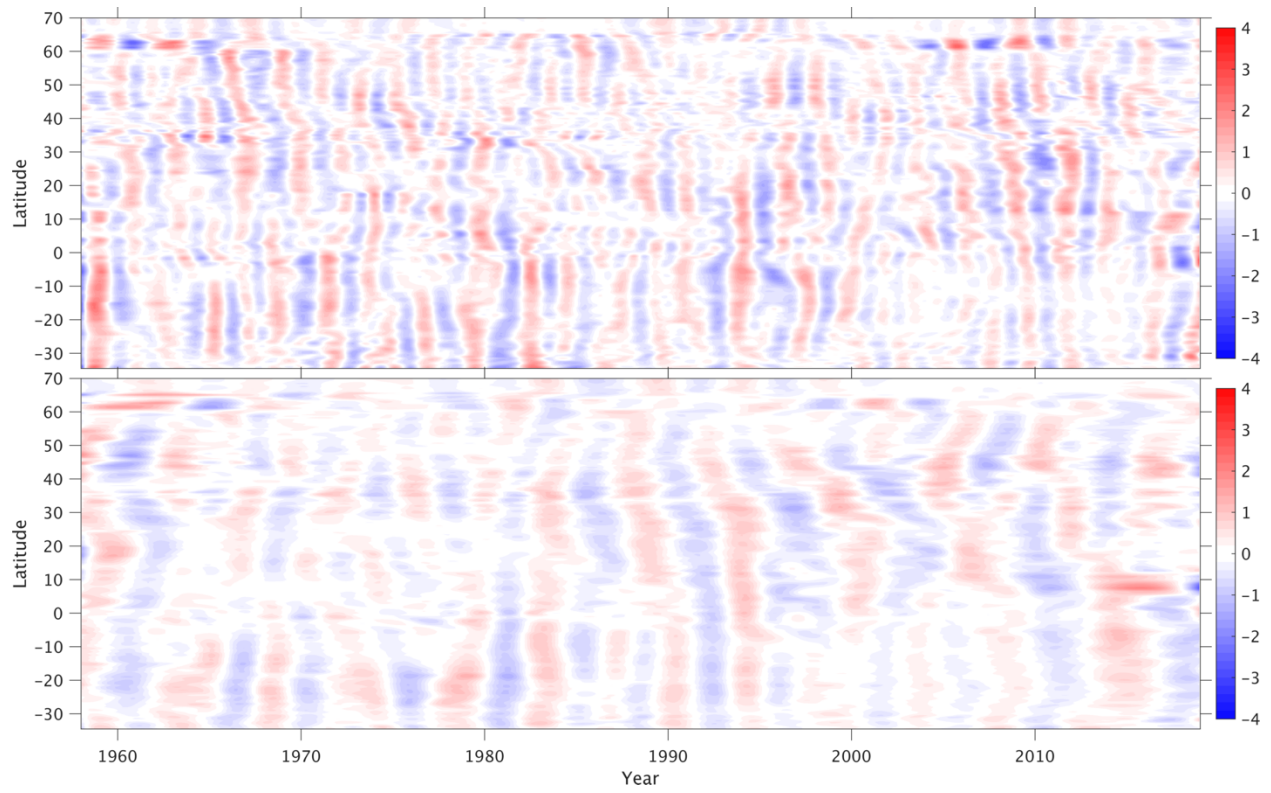


Figure 24. Modeled interannual variability of the AMOC transport (in Sv) in the Atlantic basin (35°S-70°N), based on the 4<sup>th</sup> and 5<sup>th</sup> Intrinsic mode function (IMF).

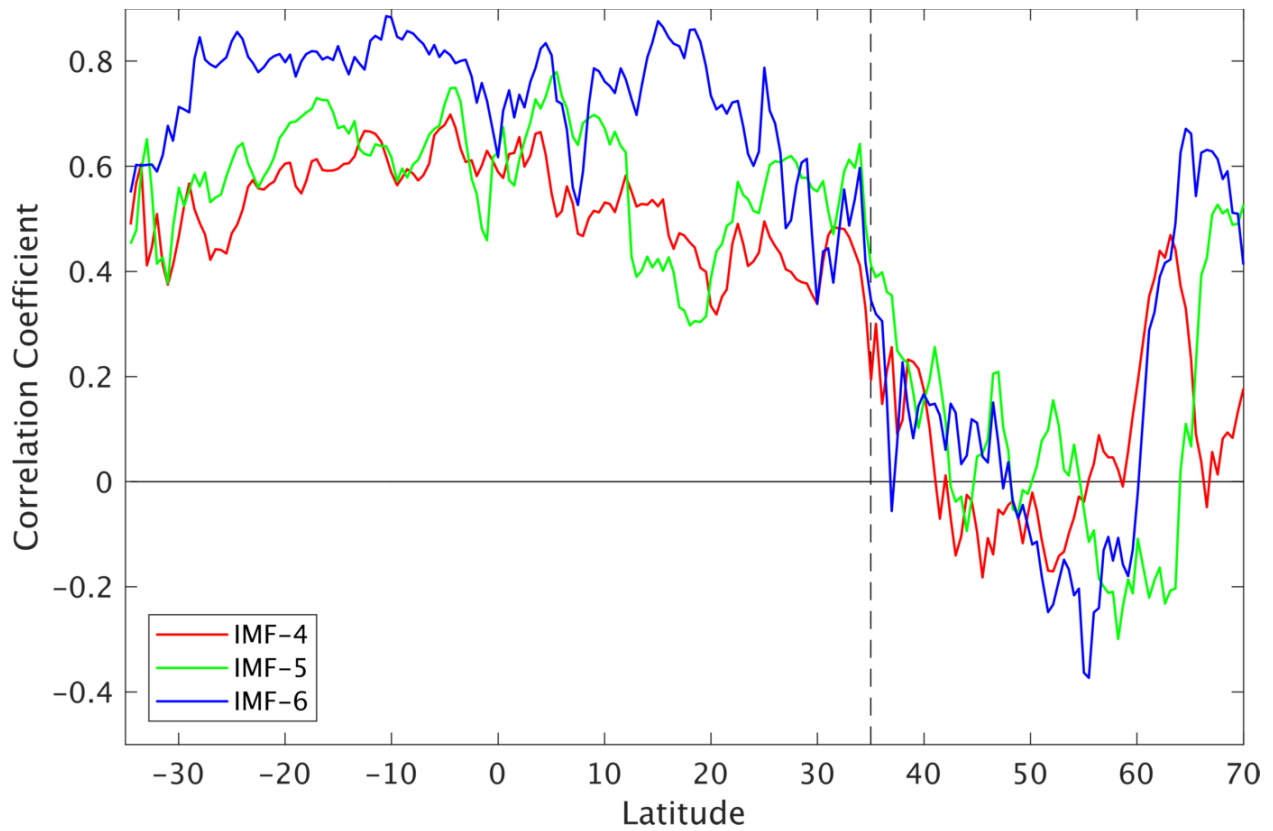


Figure 25. Correlation coefficient between the variability of the domain averaged AMOC transport and the variability of the AMOC transport at each latitude; Red and green are interannual variability (4<sup>th</sup> and 5<sup>th</sup> IMF) shown in Figure 24 and blue is decadal variability (6<sup>th</sup> IMF) shown in Figure 26.

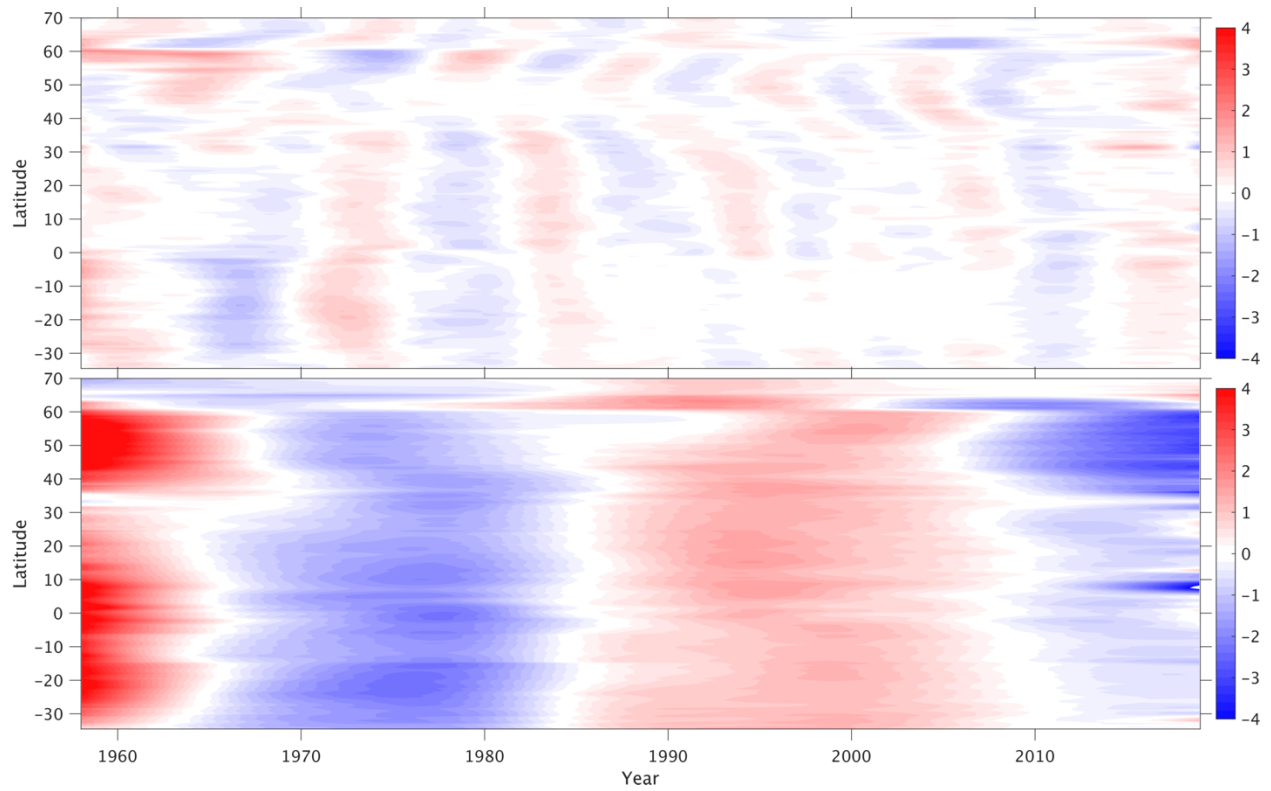


Figure 26. Modeled decadal and longer-term variability of the AMOC transport (in Sv) in the Atlantic Basin (35°S-70°N), based on the 6<sup>th</sup> and the sum of 7<sup>th</sup> to 9<sup>th</sup> Intrinsic mode function (IMF), respectively.